Neuronal cell signal analysis: spike detection algorithm development for microelectrode array recordings

Andrey Vinogradov

School of Science

Thesis submitted for examination for the degree of Master of Science in Technology.

Espoo 29.7.2019

Supervisor

Assoc. Prof. Lauri Parkkonen

Advisors

Adj. Prof. Susanna Narkilahti

M.Sc. Tanja Hyvärinen

Aalto University
School of Science

Aalto University
School of Science

Aalto University, P.O. BOX 11000, 00076 AALTO
www.aalto.fi
Abstract of the master's thesis

Author Andrey Vinogradov

Title Neuronal cell signal analysis: spike detection algorithm development for microelectrode array recordings

Degree programme Life Science Technologies

Major Human Neuroscience and Technology **Code of major** SCI3601

Supervisor Assoc. Prof. Lauri Parkkonen

Advisors Adj. Prof. Susanna Narkilahti, M.Sc. Tanja Hyvärinen

Date 29.7.2019 **Number of pages** 59 **Language** English

Abstract

Neural signal acquisition and processing techniques are rising trends among wide scientific and commercial areas. Microelectrode array (MEA) technology makes it possible to access and record the electrical activity of neural cells.

In this work, human pluripotent stem cell (hPSC) -derived neuronal populations were grown on MEA plates. The activity of the cells was recorded and the research about modern signal processing methods for the neural spike detection was performed. A list of approaches was selected for detailed investigation and the most efficient one was chosen as the new technique for permanent use in Neuro research group of Tampere University. The laboratory activities involved cell culture plating, regular medium changes, spontaneous activity recordings and pharmacological manipulations. The data acquired from the pharmacological experiments were used for the comparison between the old and new spike detection algorithms in terms of the numbers of events detected.

The Stationary Wavelet Transform-based Teager Energy Operator (SWTTEO) shows prominent performance in tests with synthetic data. The use of the proposed algorithm in conjunction with the common amplitude-based thresholding enables to lower the threshold and to detect more spikes without an excessive number of false positives. This mode is applicable for real cell data.

The detection method was considered superior and was further distributed for the processing of all neural data of the research group which included signals acquired from neuronal populations derived from human embryonic and induced pluripotent stem cells (hESCs and iPSCs) as well as rat cells.

Keywords Spike detection, neural signal processing, wavelet analysis, MEA

Acknowledgements

I would like to express my profound appreciation to my School and Prof. Lauri Parkkonen for the opportunity to pursue my master's degree. I wish to thank Neuro research group of Tampere University for accepting me, Laura Ylä-Outinen for the detailed introduction to the task, Tanja Hyvärinen and Susanna Narkilahti for their useful comments and remarks through my thesis work. I am grateful to Florian Lieb for his fast and detailed answers for my annoying questions and Mark Van Gils for his teaching and consultation.

Otaniemi, 29.7.2019 Andrey Vinogradov

Contents

Symbols and abbreviations

Abbreviations

AA	ascorbic acid
ABS	absolute thresholding algorithm
AR	autoregressive
ARMA	autoregressive–moving-average
ATP	adenosine triphosphate
BDNF	brain-derived neurotrophic factor
BMPs	bone morphogenetic proteins
c-Myc	V-Myc avian myelocytomatosis viral oncogene homolog
CNS	central nervous system
CWT	continuous wavelet transform
db-cAMP	dibutyryl-cyclic adenosine monophosphate
DNA	deoxyribonucleic acid
DWT	discrete wavelet transform
EAP	extracellular action potential
EBS	electrical brain stimulation
EEG	electroencephalography
ePSP	excitatory postsynaptic potential
FGFs	fibroblast growth factors
FP	false positive
FPR	false positive rate
GDNF	glial-derived neurotrophic factor
HBBSD	Hybrid Blind Beamforming algorithm
hESCs	human embryonic stem cells
hPSCs	human pluripotent stem cells
iPSCs	induced pluripotent stem cells
iPSP	inhibitory postsynaptic potential
Klf4	Kruppel-like factor 4
LFP	local field potential
LIN28	lin-28 homolog A
LSB	least significant bit
MAD	median absolute deviation
MEA	microelectrode array
MEG	magnetoencephalography
MTEO	Multiresolution Teager Energy Operator
NANOG	Homeobox protein NANOG transcription factor
NE	neuroepithelial
NMM	neural maintenance medium
NPCs	neural progenitor cells
Oct3/4	Octamer-binding transcription factor 3/4
PEDOT	poly(3,4-ethylenedioxythiophene) conductive polymer
PSP	postsynaptic potential

PTSD	Precision Timing Spike Detection algorithm
RGCs	radial glial cells
ROC	receiver operator characteristic
Sox2	SRY (Sex Determining Region Y)-Box 2 transcription factor
SDDT	Spike Detection Differential Threshold
SNR	signal-to-noise ratio
STFT	short-time Fourier transform
SWT	stationary wavelet transform
SWTTEO	Stationary Wavelet Transform-based Teager Energy Operator
TCF	threshold calculation factor
TEO	Teager energy operator
TGFβ	transforming growth factor beta
TIFCO	Time-frequency-based convolution algorithm
TMS	transcranial magnetic stimulation
TN	true negative
TPR	true positive rate
WNT	name of a family of secreted glycoproteins
WTEO	Wavelet-based Teager Energy Operator algorithm

1 Introduction

Revealing the brain function and organization is one of the key questions of concern for life sciences. Recent progress in stem cell research has opened an opportunity of growing functional neuronal networks in vitro. Likewise, modern achievements in the field of electronics provide a sustainable background for the extracellular signal acquisition.

A microelectrode array (MEA) plate technology is a promising scientific tool which enables culturing of neuronal populations right on top of the array of microelectrodes and regular recordings of the electrical activity of the cells. However, the obtained signal needs sufficient processing due to its noisy nature and not clearly distinguishable components. The fact that there is not much opportunity to gain any ground truth information about the ongoing cellular events makes the situation even more complicated. The goal is to apply all the knowledge of the suggested neural activity to characterize the signal and to extract valuable data. Some specific sharp voltage jumps are considered as neural events in the acquired signal and the most common approach implies amplitude thresholding techniques that are usually either embedded in the recording software or utilized separately. This method extracts amplitude outliers of the signal and designates them as neural activity events.

1.1 Demand for new spike detection approach

The usage of the simple amplitude-based thresholding for spike detection is a widespread solution. Regardless of its simplicity, low computational complexity and relative implementation clarity, this method does not show satisfactory results when the amplitude difference between the signal and noise is not clearly distinct. Moreover, static thresholding based on some signal statistics is not capable to reflect the local changes of the signal properties that happen in MEA recordings. Furthermore, the threshold calculation is not straightforward when it comes to different activity patterns under various conditions. Looking through the results of this spike detection algorithm the biologists of Neuro research group have noticed numerous misdetections of possible events within recordings. Furthermore, as the research group has started to work with the neurons derived using new protocols which tend to show more activity, the demand for a new spike detection method has become obvious.

1.2 Scope of the thesis

The scope of this work is to perform excessive literature research and to find a new suitable method for the neural event extraction and to prove that it surpasses the old one. Synthetic data tests produce a quantitative evaluation of the detection performance and some comparisons and visualizations are to demonstrate the differences in the applications of the algorithms on real data. The results of the current work are intended for more accurate characterization of the neural activity of the in vitro cell population under different pharmacological treatments. The new spike detection

algorithm will be used in the research of in vitro epilepsy modeling in the research group.

1.3 Thesis outline

Chapter 2 is devoted to all sufficient background knowledge required for understanding neural activity phenomena and its recording as well as a short introduction into the signal processing methods and algorithms considered.

Chapter 3 describes the material base of the research including equipment models and software versions.

Chapter 4 explains all the steps of the work performed.

Chapter 5 demonstrates the obtained results with visualizations and some discussion.

Chapter 6 draws a conclusion about the project.

2 Background

2.1 Brain

The brain is the most sophisticated organ in a vertebrate's body. The central nervous system (CNS) of a human comprises the brain and the spinal cord. It processes the input information and manages all the activities of the organism. The two fundamental cell types of the CNS are neurons and glial cells. Though the numbers of these cells in the brain are roughly equal, the neurons establish the tremendous diversity of the brain functioning. The neuroglia arrange structural support of the neural tissue, perform homeostasis and form the insulating myelin sheath of the myelinated nerve fibers. The neurons belong to excitable cells, the neuronal membrane is capable to conduct the nerve impulse: a transient voltage perturbation called the action potential [1].

2.2 Neuron

The main structural components of a neuron are neurites and the soma. The soma represents the cell body and the neurites are the branching processes extending out from the soma. Most somas are 0.01–0.05 mm in diameter. The inside of a neuron is filled with potassium-rich solution called cytosol. The soma accomodates the organelles of the neuronal cell, such as the Golgi apparatus, the smooth endoplasmic reticulum, the rough endoplasmic reticulum, the mitochondria and the nucleus. The excitable neuronal membrane isolates the interior of the cell from the extracellular surroundings. The neurites of a neuron include the dendrites and the axon. The dendrites form a diverging tree around the neuron and receive the input connections from the neighboring neurons. Usually, the axon is a single longer projection that conducts the generated electrical impulse away from the soma to the connection with the recipient cell. The area where the axonal fiber exits the soma is called the axon hillock. Axons may prolong from less than a millimeter to more than a meter long. The axon ends with the axon terminal. In the axon terminal the synaptic vesicles are stored. They constitute small membrane sacs filled with chemical messengers called neurotransmitters. The arrival of the action potential from the soma launches a cascade reaction causing the release of the vesicle contents from the axonal terminal into the synaptic cleft [1].

2.3 Synapse

Neurons exchange information with each other through certain contact zones called the synapses. There are two types of synapses: electrical and chemical. The electrical synapses are termed gap junctions. They make up simple channels which connect the adjacent neuronal membranes enabling the ionic current flow between the neurons [2]. The chemical synapse consists of the presynaptic axon terminal and the postsynaptic dendrite or soma segment of the innervated neuron with the synaptic cleft between them. On the postsynaptic membrane there exist the receptors which are sensitive to

the appearance of the neurotransmitters in the synaptic cleft. The action potential reaches the axonal terminal and the neurotransmitters are released consequently. These neurotransmitters bind to the receptors of the postsynaptic neuron [1].

There are two types of receptors: ionotropic and metabotropic. The ionotropic receptors embody the ionic channels in their structure. The ionic channel conductance is modulated by the binding of a particular neurotransmitter with the receptor. On the contrary, the metabotropic receptors adjust the behavior of the ionic channels indirectly, via certain chemical cascades inside the cell [1].

The opening or closing of the postsynaptic ion channels results in the depolarization or hyperpolarization of the postsynaptic neuron, generating excitatory postsynaptic potential (ePSP) or inhibitory postsynaptic potential (iPSP) respectively [1]. That is how the activity of the postsynaptic cell is stimulated or suppressed.

2.4 In vivo and in vitro research

The research of the human brain development and functioning has been constrained for years by low accessibility of the living tissue for the analysis in vivo [3, 4]. The post-mortem studies may reveal structural arrangement features of the brain but the feasible insight into its functional specifics is limited for this approach.

This restraint can be partly solved by obtaining living brain slices for the in vitro analysis [5], but this technique also has its limitations, such as an obvious damage of the tissue during the slicing procedure, the degradation of the prepared living tissue and inapplicability of the idea to the human brain due to self-evident reasoning.

Recently the pluripotent stem cell-based protocols have been elaborated which make possible the creation of alive neural cell populations in vitro. This fact opens up new horizons for the investigation of brain development and impairments as well as for the exploration of its functionality [4].

2.5 Stem cells

Stem cells are the cells that are capable of self-renewal and production of all cell types in a particular tissue or in a whole organism. These properties of the stem cells remain during long periods of the host life [6]. There are four levels of the stem cell differentiation potential: totipotent, pluripotent, multipotent and unipotent cells. The example of the totipotent stem cell is a fertilized egg, a zygote, which is able to engender an entire organism [6, 7]. During the following mitotic cell division of a zygote, the next developmental stages appear: a morula, the bunch of totipotent cells (blastomeres), and next – a blastula.

For mammals, the blastula stage is associated with a blastocyst, the structure which consists of an embryoblast surrounded by a trophoblast. All the tissues of the fetus develop from the embryoblast or so-called the inner cell mass while extra-embryonic tissues, such as placenta, are formed from the trophoblast [8]. The inner cell mass comprises the pluripotent stem cells. These cells are able to differentiate into all the cell types of an embryo but can not generate the trophoblast cells [6]. Considering the human blastocyst, these cells are the source of human embryonic

stem cells (hESCs). They are capable of the generation of more than 200 cell types of the human body (with some specific stimulation achieved) [9], including neurons and glia.

But due to the fact that the blastocyst has to be destroyed to obtain the human embryonic stem cells some parts of the society raise ethical discussions around this procedure [6]. The embryos at the blastocyst stage may be received from volunteers as there sometimes remain some unused samples (low-quality embryos usually) from in vitro fertilization treatments [10].

In 2007 two research groups reported about the successfully implemented transformation of the adult human somatic cells into the pluripotent stem cell stage in a way that they showed the same main properties as the human embryonic stem cells [11, 12]. These researches involved cell DNA modification by retrovirus transduction of the following transcription factors: Oct3/4, Sox2, c-Myc, and Klf4 [11] or Oct4, Sox2, NANOG, and LIN28 [12].

Further research explored that it is also possible to reprogram the cells directly passing over the induced pluripotent stem cell stage [3]. All in all, two types of cells make up the human pluripotent stem cells (hPSCs), the immense source of research and progress: the human embryonic stem cells (hESCs) and the induced pluripotent stem cells (iPSCs).

2.5.1 Development in vivo

To understand the principles of the differentiation of neurons from the hPSCs it is crucial to look through the basics of the developmental neurobiology. During the second week of the embryonic development, the inner cell mass of the blastocyst mentioned above differentiates into two layers: the hypoblast and the epiblast forming a bilaminar disk. Then the gastrulation stage starts with the trilaminar disk of the three germ layers (endoderm, mesoderm and ectoderm) produced at the end. Next, during the neurulation phase, a neural plate appears in the ectoderm layer and through the descending of the neural plate into the mesoderm and the creation of a cylindrical structure the neural tube is formed [13]. The walls of the neural tube give rise to the whole CNS [1].

The ectodermal cells are able to differentiate into neural or epidermal cells [14, 15]. For vertebrates, the fate of the ectodermal cells starts being determined already during the gastrulation [14]. Certain extrinsic chemical factors called morphogenes bind to the extracellular receptors of a cell and initiate the cascades of internal reactions ending up with activation of particular genes of DNA in the nucleus.

The default pathway model states that the morphogenes force the ectodermal cells to epidermal fate and/or act as inhibitors of neural fate and that the neural developmental path is the default for the cells if no chemical signaling is presented [14]. Hence the trigger of the cell fate could be either the presence of the morphogenes or the absence of them.

The main factors that influence the direction of differentiation of the ectodermal cells are the transforming growth factor beta (TGFβ) family of proteins which include bone morphogenetic proteins (BMPs), activin and Nodal proteins. There are multiple

pieces of evidence that the inhibition of these signaling pathways induce neural fate of the ectodermal cells [14–16]. Recently the confirmation of the role of glycoproteins fibroblast growth factors (FGFs) and WNTs in neural induction has been discovered [15, 16]. The presence of certain factors (affecting cell fate) is spatiotemporally controlled in the developing organism [16]. The neural fate initiation is called neural induction [4].

Neuroepithelial (or neuroectodermal) cells (NE cells) that constitute the neural plate and early neural tube are primary neural progenitor cells (NPCs), they divide symmetrically at first but as the neural tube closes and the neurogenesis starts the neuroephitelial cells begin to divide asymmetrically producing neurons and secondary neural progenitor cells: radial glial cells (RGCs) and basal progenitors [3, 17]. Thereafter, during the following development, the most neurons and glia are generated from the radial glial cells [3].

2.5.2 Human pluripotent stem cell-derived neurons

The neuronal differentiation in vitro involves the neural induction with neural progenitor cells (NPCs) as the result and neuronal maturation phase [18, 19]. The neural induction of pluripotent stem cells in vitro is targeted to mimic key molecular and cellular aspects that that happen in vivo [4, 18]. Most modern protocols of the neural induction of the hPSCs usually suggest culturing without the morphogens and/or with the inhibitors of the Nodal/Activin and BMP pathways [4]. The neural induction aims at the generation of neuroepithelial progenitor cell populated areas called neural rosettes [4, 18], which mimic neural tube formation in vitro [20, 21]. The scheme of the neural induction in the culture of the pluripotent stem cells is depicted in Figure 1. The generated neurons are used for extensive developmental research [3, 4] including electrophysiological experiments [19].

2.6 Cellular electrophysiology

2.6.1 Resting state membrane potential

The animal cells are encapsulated in a membrane which consists of a phospholipid bilayer with protein inclusions. The two molecules thick membrane has long non-polar hydrophobic chains of hydrocarbons inside its structure and hydrophilic phosphate groups on its both surfaces [1]. The neuronal membrane prevents the cell contents from diffusion effectively isolating the inside cell potassium-rich solution called the cytosol from the extracellular fluid [1]. The membrane functions as an insulator and a diffusion barrier to the movement of ions, the main charge carrying units in biological systems [1].

There exists a sustained difference of electric potential across the membrane of a neuron termed the resting potential which is maintained by a particular distribution of positive charge ions, cations, and negative charge ions, anions [22]. It is about $-65\,\mathrm{mV}$ for neurons in a resting state [1]. This transmembrane potential may change due to the number of factors such as acidity, temperature, extracellular concentrations of ions, extrinsic electric stimuli and others [22]. It is important to remark that the

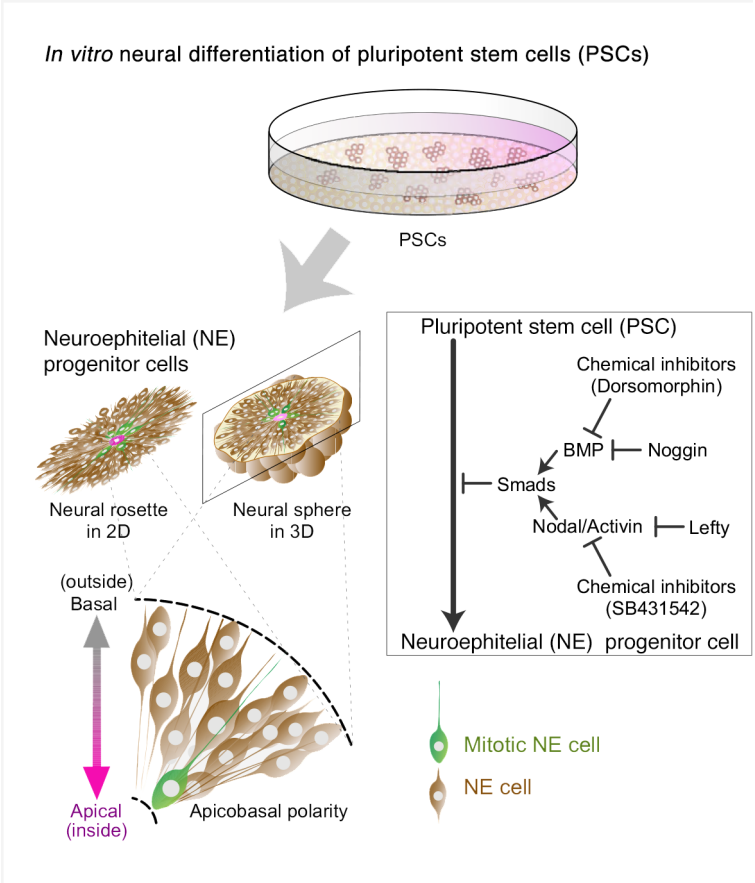

Figure 1: Neural induction in vitro. Adapted from [4].

system as a whole has a neutral electric charge because the unbalanced charges inside and outside of the neuron arrange on the opposite sides of the cell membrane [1].

The most important ions involved in the functioning of the neuronal cell are cations of sodium, potassium, calcium and magnesium and anion of chloride [1]. There are two causes of ion movements: the concentration gradients and the electric force. The first one drives ions down their concentration gradients and the second makes them drift towards the pole of an opposite sign. When these two factors are counterbalanced for a certain ion the Nernst equilibrium potential is achieved. The Nernst equilibrium potential for a particular ion is calculated in accordance with the Nernst equation. The equation considers concentrations but does not take into account the selective permeability of the neuronal membrane [1]. The inner cell concentration of potassium is about 20 times greater than outside of the cell. The Nernst equilibrium potential for potassium only assuming free permeability of the membrane and twenty-fold concentration difference is about $-80\,\mathrm{mV}$. On the contrary, the concentration of calcium and sodium is higher outside of the cell, for sodium it is about nine times more [1].

There are embedded proteins in the structure of the membrane which constitute ion channels. The membrane permeability in the resting state of a neuron is guided by so-called leakage channels, the channels with more-or-less constant permeability

[22]. But particular membrane channels provide selective permeability for particular ions only and to a certain extent, so the membrane is not a free passage for all the ions [1]. The corresponding resting state membrane permeability is high for potassium and minor for sodium. Other ions do not contribute much to the resting membrane potential because even though they may have strong concentration gradients the membrane permeability for them is insufficient. It is possible to calculate the resting membrane potential concerning the relative ion concentrations and permeabilities using the Goldman equation. So if relative permeability is 40 times more for potassium than for sodium assuming the relative concentrations of these ions mentioned above the resting membrane potential will result in $-65\,\mathrm{mV}$ which is very close to reality [1].

The fact that still requires the description here is the inner negative charge source of neurons which compensates the presence of potassium cation in high concentration inside the cell. This negative charge arises from the anions of proteins and amino acids inside the neurons [22].

Other important contributors to the maintenance of the resting membrane potential are the proteins called ion pumps. They utilize energy to pump ions across the membrane against their concentration gradients. For example, sodium-potassium pump breaks down adenosine triphosphate (ATP) and pushes potassium inside from the outside of the cell and internal sodium away from the cell (3 ions of potassium and 2 ions of sodium per cycle), preserving the appropriate internal concentration of potassium [1].

The perturbation from the resting state happens due to the opening or closure of the specific ion channels in the neuronal membrane. There are two major types of ion channels: voltage-gated and ligand-gated [1, 2]. The receptors mentioned in Section 2.3 affect ligand-gated ion channels: the modulation of the channel conductance occurs due to the binding of a particular neurotransmitter with the receptor. This modulation can happen either directly or via the chemical cascades depending on the type of the receptor involved [1]. On the other hand, the voltage-gated ion channels change their state with regard to the transmembrane voltage [1]. There exists evidence that both types of channels have more than two states. It means that they may exhibit not only opened and closed condition, but also some intermediate behavior [2].

2.6.2 Action potential

A neuron is an excitable cell. It is capable of performing the rapid voltage jumps called action potentials [22]. The encoding of the information in the CNS is realized in terms of the frequency and pattern of the action potentials fired among the population of neurons [1].

Due to sufficient (above threshold) depolarization of the inside of a neuron which may be caused by the ePSP or by some extrinsic electric stimulus the excitable neuronal membrane conducts a transient voltage jump along the axon. As it has been mentioned, the interior surface of the neuronal membrane is negatively charged with respect to the outer. The action potential is a short-term reversal of this condition

which propagates from the soma to the axon terminal [1]. The action potential is caused by a sequence of voltage- and time-varying changes of the ionic channel conductances [2].

In short, as the cell is depolarized to the threshold there happens a transient increase of the sodium conductance through the sodium voltage-gated channels. This event makes up the rising phase of the action potential with the sharp depolarization caused by sodium influx.

During the overshoot stage of the action potential the transmembrane voltage reaches its peak, the sodium conductance (and consequently the sodium influx) saturates. Closer to the peak the potassium voltage-gated channels increase their conductance and the resulting potassium efflux starts to reverse the dynamics of the membrane voltage. At the falling phase of the action potential, the sodium conductance is inactivated (leaving very low permeability) while the potassium conductance attains its maximum. The negative membrane potential restores. During the undershot stage, the sodium conductance is still very low while potassium is still capable to leave the cell. It causes the membrane potential to go towards the potassium equilibrium potential: it hyperpolarizes lower than the resting state potential.

The closure of the voltage-gated potassium channels together with the sodium-potassium ion pumps activity that takes place all the time returns the membrane potential to the resting state. Due to the sodium conductance inactivation, the cell can not fire another action potential for some period until it reaches sufficient re-polarization and the sodium channels are re-activated. This period is called a refractory period [1, 22]. The propagation of the action potential happens due to the local over-threshold depolarization in the area adjacent to the one where it has already occurred [1].

In 1952 two English biophysicists Alan Lloyd Hodgkin and Andrew Fielding Huxley created the continuous-time model that quantitatively related the dynamics of the ionic channel conductances to the transmembrane potential and time [22]. Thus, their model explained the initiation and propagation of the action potential. The model describes the neuronal membrane as a parallel circuit of the capacitance (which represents non-permeable segments of the cell membrane), the time- and voltage-dependent sodium and potassium conductances and the leakage conductance (which represents the total free movement of ions through the membrane). The circuit scheme is depicted in Figure 2.

The electric phenomenon of the action potential (from a single neuron or thousands superimposed) is measured by modern neuroimaging modalities such as electroencephalography (EEG) and magnetoencephalography (MEG) and this is the event that transcranial magnetic stimulation (TMS) and modifications of electrical brain stimulation (EBS) layouts try to induce.

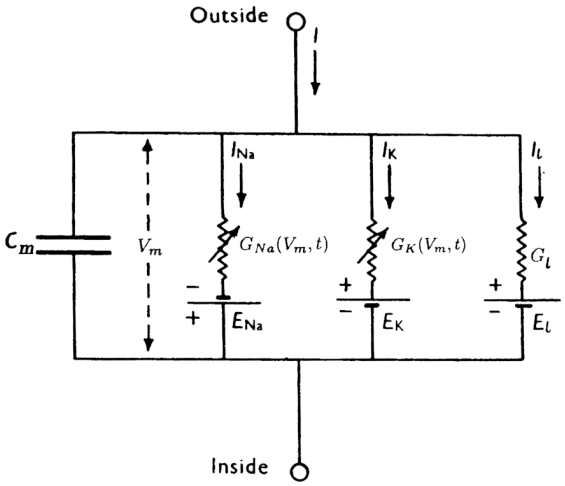

Figure 2: The Hodgkin–Huxley model of a membrane patch. The Is are transmembrane currents, the Es are the equilibrium potentials for Na and K ions as well as for the total membrane leakage, C_m is the specific capacitance of the membrane, and the Gs are specific ionic conductances. Modified from [23].

2.7 Microelectrode array

2.7.1 Microelectrode array layout

The electrical character of neuronal signaling gives an opportunity to catch the signals with the electrodes away from the origin (within certain proximity from it) [24]. "This can be achieved by the use of microelectrode arrays – a well-accepted method enabling stimulation and recording of bioelectricity with high spatial and temporal resolution in cell and tissue cultures – Microelectrode array (MEA)", as Stett and colleagues (2003) state [25]. MEA system layout comprises the conductive extracellular volume (medium in the MEA well), the substrate with the integrated electrodes (MEA well bottom), the hardware connected to the electrodes, including amplifiers, filters, a digitizer, data transmission wiring and a stimulator (MEA plate circuits, MEA headstage and computer connections) [24, 25]. The MEA plates are usually made as portable devices for comfortable culturing in cell incubators, medium changes in laminar hoods and microscopic investigation of the cells. The plate is placed on and connected to the MEA headstage only for recording periods.

The Multichannel Systems MEA 2100 recording environment may be considered as an example. The system includes various possible MEA plates with different electrode positioning/density for culturing of a cell population, the headstage with the amplifiers and stimulator circuits embedded and the interface board to connect the whole system to the computer. The system is depicted in Figure 3. The main goal of multi-electrode array recordings is to describe the interaction between neurons and its modulation in response to some stimulus [25].

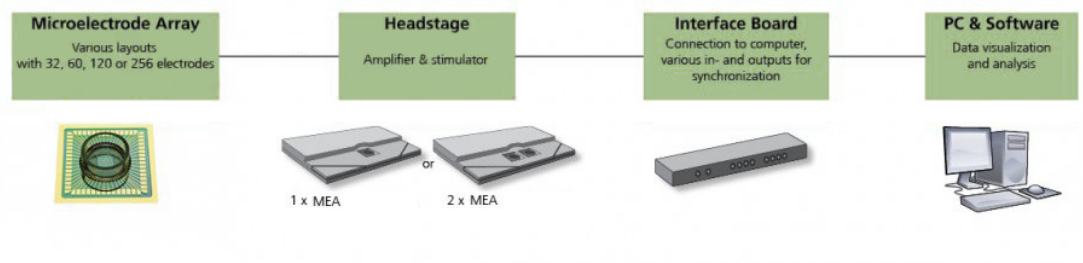

Figure 3: MEA2100-System produced by Multi Channel Systems MCS GmbH. Modified from [26].

2.7.2 Microelectrode array signal

The MEA systems give an opportunity for long-lasting and repeated extracellular recordings of the activity of neuronal populations as well as for electrical stimulation of the cells [24]. In contrast to the single-cell/single-channel resolution of the patch clamp technique (microscale), MEA records the signal of all possible sources around every sensor thus representing the mesoscale electrophysiological research [24, 27]. Each microelectrode captures the perturbations in the extracellular electric field produced by ionic currents occurring in the vicinity. These currents may originate not only from active neuronal transmembrane channels [28]. The impact of the ionic transmembrane currents on the electric field and as the result on the potential value captured by the microelectrode relies upon many factors such as the magnitude of the currents, their distance from the recording location and the sign of these currents [24]. The neuronal compartments generate these currents due to changes in the conductances of the ion channels embedded in the neuronal membrane. The duration of these extracellular field potential fluctuations is approximately equal to the transmembrane current timing [2, 25].

As it was mentioned above the action potential is the transient voltage jump which happens when the transmembrane potential attains a threshold as the result of some stimulus, chemical or electrical [24]. In neuronal signal processing, the short segment of the recording which constitutes a possible action potential is called a spike. When MEA signal waveform displays rapid voltage perturbation that exceeds certain visual threshold it is considered to represent extracellular action potential (EAP) [24].

The dynamics of the intracellular action potential (IAP) involves fast initial sodium influx resulting in a sharp increase of the transmembrane voltage which is followed by potassium efflux and corresponding voltage drop. The amplitude of these voltage oscillations lies within tens of millivolts. On the contrary, the EAPs start with negative steep and switch to positive pitch after. Their range spreads over tens to hundreds of microvolts [24]. Both IAPs and EAPs have nearly the same duration about two milliseconds or less [28]. While to detect the IAPs the direct connection to the inside of a neuron is required, the EAPs are available for recording in the close proximity to the source from the outside of the cell [24]. The electrodes are able to detect the activity up to 100 µm away [29, 30], though usually the main portion of

the signal comes from the sources located within 30 µm from the electrode center [25]. These numbers are approximate, the actual sensitivity of the electrode depends on many factors such as electrode material, MEA circuitry, etc. The typical electrode locations for detecting EAPs are perisomatic areas of neurons and axon hillocks [24].

Egert, Heck and Aertsen (2001) state that spike polarity reflects the location of the recording MEA electrode with respect to the signal source, it is negative near the soma and positive close to the dendritic tree [30]. Moreover, with the increase of the distance from the source to the electrode the amplitude of the acquired signal decreases. It might result in the situation when the spike amplitudes can not be clearly distinguished from the noise [31]. The recorded signal vary from location to location because in the recorded signal sources linearly sum up with the input of each source weighted inversely proportional to its distance from the electrode [27].

The superimposed potentials of vast cell populations generate low-frequency contributions in the recordings called local field potentials (LFP). The LFPs likewise may comprise valuable insight into the cell network functioning such as postsynaptic potentials (PSPs) of neuronal populations [25], though extracting of such information from the signal is a big challenge, and the main focus in the most MEA research is made on the EAPs.

The LFP spreads over the low-frequency band of the recorded signal spectrum: below 300 Hz [28, 32]. The processing of EAPs starts after filtering out the LFPs. The spikes reside in the 300–3000 Hz part of the signal spectrum [33]. Hence MEA signal contains slow LFPs and fast spikes of EAPs [25]. For fast events, the transmembrane current and therefore the extracellular recording is roughly equal to the first derivative of the transmembrane potential [2]. For slow events this approximation does not hold. The waveforms of the described signals are presented in Figure 4.

In MEA well microelectrodes are placed close to the cells to record the extracellular electric potential changes produced by ionic transmembrane currents. Thus the cell may be assumed as an arrangement of ion currents (and sinks) [34]. It is possible to approximate them as monopolar point sources [27, 34]. Hence, under the assumption that the cell-containing medium is homogeneous, isotropic (having identical values of a property in all directions), ohmic and has infinite spatial extension (unbounded) the voltage captured by the electrode can be solved analogously to the calculation of the potential due to point charges in free space: the Coulomb's law (with with the charge q replaced by the current I) [27, 34, 35]. For a single point source:

$$V_e = \frac{I}{4\pi\sigma r}, \tag{1}$$

where I is the amplitude of a point source of current (A), and r is the distance from the source to the measurement point (m), and σ is the conductivity (S/m) of the extracellular medium. In a case when N point sources are considered, that is, source regions with volumes much smaller than the distances to recording electrode, the extracellular potential resulting from the multi-compartment model is given by:

$$V_e = \frac{1}{4\pi\sigma} \sum_{n}^{N} \frac{I_n}{r_n}, \tag{2}$$

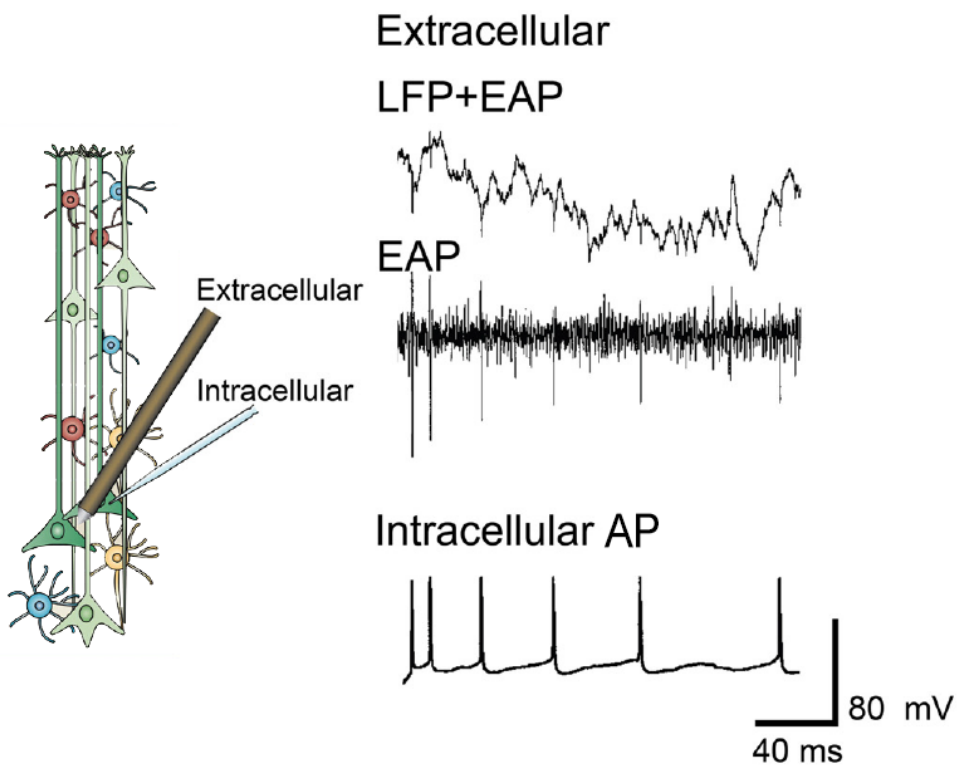

Figure 4: The waveforms of the intracellular action potential (IAP), the extracellular action potential (EAP) and the EAP with the local field potential (LFP) superimposed. Modified from [24].

where I_n represents the n^{th} monopolar point current source, r_n - the distance between the point source and measuring field point (the recording electrode), and N is the number of individual point sources [27, 34, 35].

Though the biophysical background is similar for any kind of such extracellular recording, the research focus can be made on different constituents of the signal. The records may be investigated for individual spikes of a single cell, for spiking activity of multiple cells and for the local field potential dynamics [25].

Previously, the most neuronal populations cultured on MEA plates were two-dimensional. However, there is a trend of cultivation of functional three-dimensional cell cultures on MEAs [36, 37]. The challenge lies in the fact that these 3D networks appear to produce lower spike amplitudes and smaller signal-to-noise ratio (SNR) [31].

2.7.3 Noise

The background noise in MEA recordings is correlated as it has distant spiking in its origin [38]. The main noise contribution comes from distant cell electrical activity such as action potentials and subthreshold events [24, 39]. Therefore, the signal and noise spectra also overlap [38–40]. Though this component of the signal might carry information about important cellular phenomena [25] as it was mentioned above, for

spike analysis it is usually considered undesirable biological noise and filtered out [24].

Besides the noise of the biological origin, the liquid-metal interface contributes to the noise as well [24]. In the lower part of the spectrum there exists 1/f noise [24, 40, 41]. Moreover, thermal noise adds to all of this [24]. Small electrodes are utilized in the MEA for high spatial resolution. Unluckily, the thermal noise has an inverse correlation with the electrode size [42]. Another noise contributor in MEA recordings is the 50–60 Hz power line interference, which enters the signal generally between the microelectrode and its connection to the amplifier [24].

Finally, the hardware components of the MEA system corrupt the signal by noise. The amplifiers themselves add some noise portion. Furthermore, the quantization performed by the analog-to-digital converter contributes to the noise. The quantization noise may be approximated by the factor of $\sqrt{1/12}$ multiplied by the least significant bit (LSB) magnitude [24]. In addition, the phase noise can be mentioned which originates from the difference in timing of an actual action potential occurrence and its digitization [41]. The quality of the signal might be affected by any lossy compression techniques involved in data transmission [24]. Figure 5 shows the noise contributors in MEA recordings.

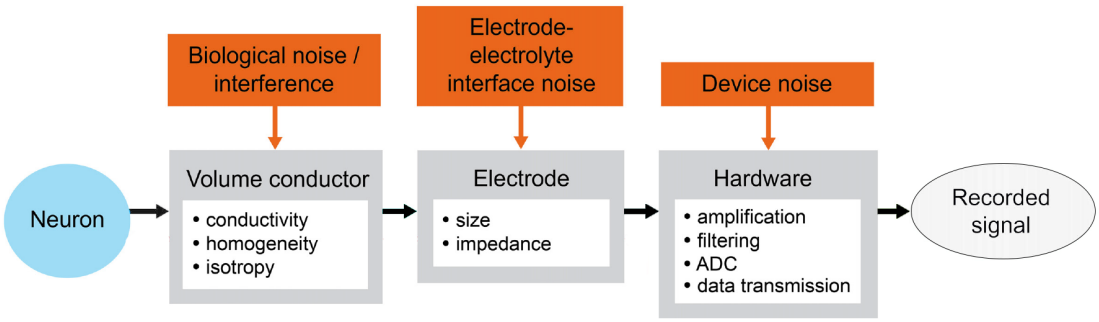

Figure 5: The MEA signal noise contributors. Modified from [24]

2.8 Neuronal signal processing

The biosignals acquired based on the electric nature of the brain activity are non-stationary, non-periodic (with possible quasi-periodic fractions) and noisy. The basic signal processing activities for the neural data include spike detection and sorting, burst detection and synchronous activity analysis. The bursts are dense sequences of spikes in a signal. The current work is focused on the spike detection: the extraction of EAPs from the raw MEA signal. The most frequent approach in this field comprises simple band-pass prefiltering with subsequent thresholding [31, 43]. Aside from its simplicity and low computational complexity, this method has

some serious disadvantages: it begins to fail when spike amplitudes do not differ significantly from the noise amplitudes [31].

The typical procedure in signal processing to gather some information from the waveform is to project it on a set of basis functions[43, 44]. The Fourier transform which constructs the frequency domain representation of time series via the decomposition of the signal into a sum of sinusoids lacks time resolution: it is possible to see the frequency contents of the signal but it is very difficult to localize particular signal components in time. The timing information is embedded in the phase part of the Fourier transform and it is very difficult to solve such encoding: a particular event in time spreads over all phase components, a local feature in time is transformed into a global feature in phase [45]. Moreover, classical spectral methods such as the Fourier transform, require signal stationarity assumption for satisfactory performance [45]. The MEA signal, as well as many other signals of biological origin, is clearly non-stationary, thus, it exhibits substantial changes of its statistical properties over time.

A variety of techniques have been proposed to acquire the localized characteristics of a waveform in both time and frequency domains. These approaches are called time-frequency analysis methods [45]. The first and the most obvious solution is to separate the analyzed waveform into short portions (windows) and perform the analysis of each of them individually with the standard Fourier transform. This method is called short-time (or short-term) Fourier transform (STFT). The STFT offers a trade-off between the time and frequency resolution: with the increase of the analyzed segment length the frequency resolution increases but the time clarity reduces and vice versa [45].

Another representative of time-frequency analysis methods is wavelet transform, sometimes referred to as time-scale approach. The wavelet transform is another option for obtaining both time and frequency characteristics of a waveform but instead of the separation into the time segments, the division into segments of scale is performed [45]. The two fundamental benefits of this technique are optimal resolutions in both time and frequency and the fact that no signal stationarity assumption is required [43].

In the wavelet transform the basis of functions is utilized for the decomposition as well but all the members of this basis are represented by dilated or compressed variants of some base (probing) function. This base function is a finite compact wavelike function, its form can be expressed as a damped oscillation and it is called a wavelet [45]. While the Fourier basis of complex exponentials performs well for smooth signals but tends to operate poorly in case of presence of transients and discontinuities in a waveform, wavelet bases are more flexible as they are capable of adaptation to local signal behavior. Narrow scales of a wavelet cover high-frequency segments while its wide scales cover low-frequency regions [46]. This property results in high efficiency of non-smooth signal decomposition.

The main advantage of wavelets in the field of neuronal signal processing is that wavelet basis functions have biphasic, triphasic and multiphasic waveforms with compact support and consequently they resemble the shape of the action potentials. "The basis function dilated over many scales acts as a number of effective

approximations of the matched filter at some particular scales even though the exact waveform of the action potential is not known" as Nabar and Rajgopal (2009) state in their work [38].

2.8.1 Mathematical background

Continuous Wavelet Transform

The wavelet transform constitutes multiresolution time-frequency analysis of the waveform of interest with the scaled and shifted versions of a mother wavelet. The continuous wavelet transform (CWT) can be considered as the inner product of the signal f with scaled and shifted versions of the mother wavelet Ψ, where f is a quadratically integrable function [38] or so-called finite-energy function:

$$W(a,b) = \int_{-\infty}^{\infty} x(t) \frac{1}{\sqrt{|a|}} \Psi\left(\frac{t-b}{a}\right) dt, \tag{3}$$

where b expresses the shift across the signal and a represents the scaling of the wavelet. The obtained coefficients $W(a,b)$ explain the correlation between the signal and the wavelet at various positions and scales. Thus the particular coefficient shows their degree of similarity at the wavelet location b and its scale a. Hence, the wavelet transform performs a sliding correlation analysis of the input waveform and the translated and dilated versions of a reference template called the mother wavelet Ψ. The resulting coefficients would have local peaks where the signal is most accurately reconstructed by the wavelet [38, 45]. The CWT is highly redundant, which means that a much bigger number of coefficients is generated than it is required to uniquely characterize the signal [45].

Discrete Wavelet Transform

The version of the wavelet transform that is widely applied in digital signal processing is called a discrete wavelet transform (DWT). To overcome the redundancy of the CWT and to achieve the result with the same number of data points as in the input signal the decomposition is limited by logarithmic discretization. The most common way is to use the powers of two for this restriction. This version of the DWT is called a dyadic wavelet transform. The formula below shows signal representation via DWT coefficients and is presented below:

$$d(k,l) = \int_{-\infty}^{\infty} \psi(2^k t - l) f(t) dt. \tag{4}$$

And signal representation via DWT coefficients and a wavelet function is presented below:

$$f(t) = \sum_{-\infty}^{\infty} \sum_{-\infty}^{\infty} d(k,l) 2^{-k/2} \psi(2^{-k} t - l), \tag{5}$$

where k is related to a as $a = 2k$, b is related to l as $b = 2kl$, $d(k,l)$ is a sampling of $W(a,b)$ at discrete points k and ψ is the wavelet function [45].

In most digital signal processing cases, the DWT is implemented in the filter bank format. It means the usage of multiple filters to separate the waveform of interest into different subbands. This process is called subband coding [45]. The concept relies on the application of the basis functions to perform the analysis at coarse and fine resolutions hence the term multiresolution analysis is used. The coarse resolution analysis or low-pass filtering is achieved with the application of a father wavelet or a so-called scaling function. The result of this operation is approximation coefficients which represent lower frequency content of the waveform of interest. The fine resolution analysis or high-pass filtering constitutes the operation of a mother wavelet or a wavelet function with the detail coefficients representing higher frequency contents of the signal as the result. The wavelet function can be obtained from the scaling function. The downsampling is performed after both analyses. The scaling and wavelet functions are then applied to the downsampled approximation coefficients moving the decomposition to the next level:

$$c_{D/A}(t) = \sum_{n=0}^{L-1} f(n)\psi_{D/A}(2t - n), \tag{6}$$

where $f(n)$ denotes the analyzed signal, $\psi_{D/A}$ expresses either the high-pass wavelet filter yielding the detail coefficients c_D or the low-pass filter resulting in the approximation coefficients c_A. This procedure may be iterated k times by replacing the input f with the approximation coefficients c_A of the previous decomposition [31]. The single-level decomposition is displayed below:

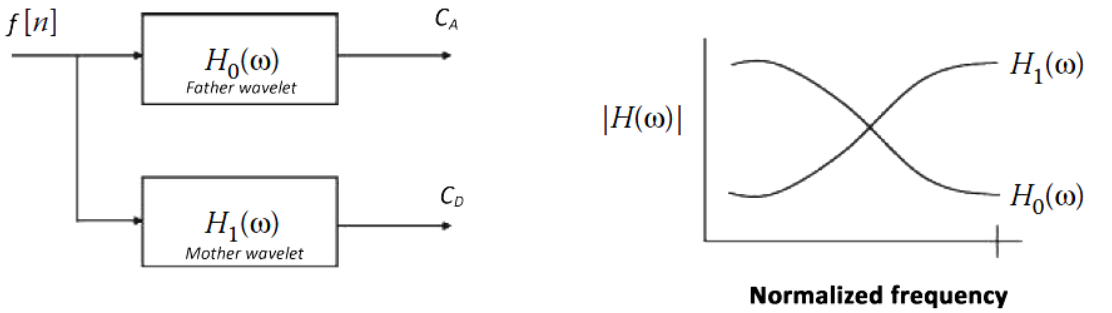

Figure 6: A single level filter bank consisting of only two filters applied to the same waveform. The filters have lowpass and highpass spectral characteristics: the outputs are a lowpass subband, C_A, and a highpass subband, C_D. Adapted from [45].

In this version of the DWT the scaling of the mother and father wavelet functions themselves is not performed, the effect of scaling is rather achieved by the downsampling. The downsampling causes the main substantial disadvantage of the classical DWT: it is not a time-invariant transform which means that the DWT of a signal and the DWT of the same signal shifted in time do not differ in the shift of the coefficients only [31].

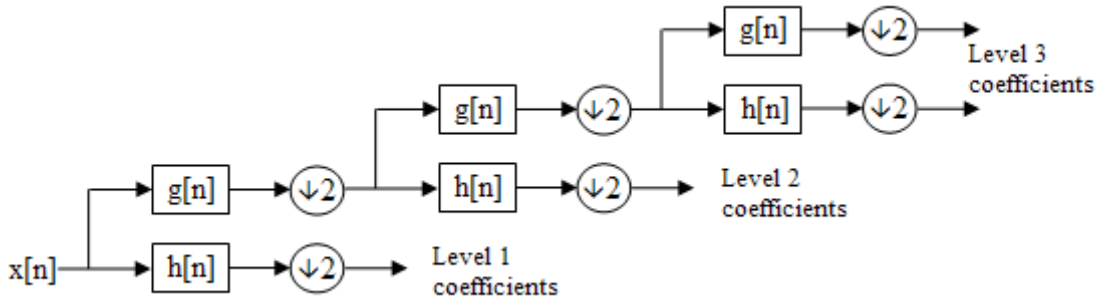

Figure 7: A DWT filter bank of level 3. The downsampling by a factor of 2 is performed after the convolution with each level filters. Retrieved from [47].

Stationary Wavelet Transform

A stationary wavelet transform (SWT) is a redundant time-invariant version of the DWT. The downsampling of the filter outputs is removed from the DWT algorithm and the upsampling of the filter coefficients is performed instead. Hence, the size of the input at each level stays intact and each filter is upsampled by a factor of $2^{(j-1)}$ in the jth level of the decomposition by zero padding [31, 48, 49]. The structure of the SWT filter bank is depicted in Figure 8.

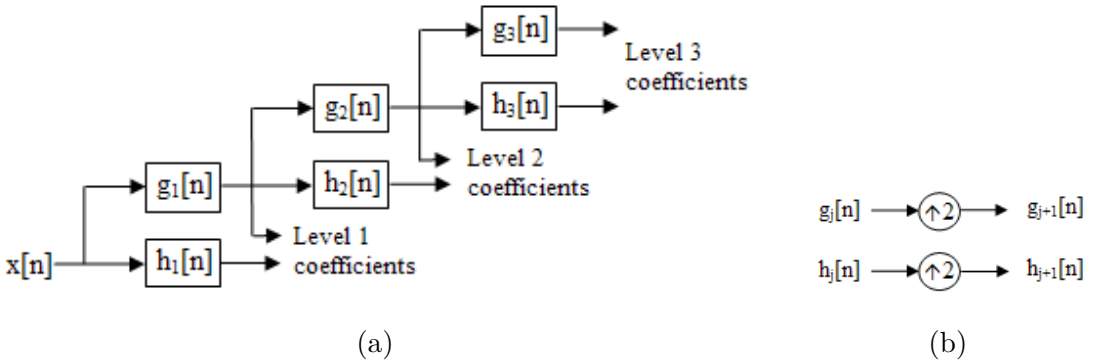

Figure 8: (a) A SWT filter bank of level 3 (b) The upsampling of the filters for the next level of the decomposition. The schemes are retrieved from [50].

The redundancy of the SWT comes from the fact that the output of each level of the decomposition consists of the same number of samples as the input signal.

Teager Energy Operator

Another useful signal transformation technique is a Non-linear Energy Operator (NEO) also called the Teager–Kaiser Energy Operator (TKEO) and the Teager Energy Operator (TEO) in some sources [51, 52]. In the current work the Teager Energy Operator (TEO) notation is used.

For the sinusoidal input, the TEO output is proportional to the square product of the instantaneous amplitude and frequency of the signal [40, 53]. The instantaneous amplitude and frequency are the amplitude and frequency of the superior sinusoidal component of the signal at a particular time point. The method has modest computational load and does not require any prerequisite knowledge about the input signal [40]. It emphasizes high-frequency signal components concentrated in a short time interval [52, 53]. The discrete TEO is calculated by taking the difference between the squared signal value at the current time point and the product of its neighbor samples, as it is shown in the formula below:

$$\Psi\{x(n)\} = x^2(n) - x(n-1)x(n+1), \tag{7}$$

where $x(n)$ is the input waveform.

2.8.2 Spike detection algorithms

There are many spike detection approaches published throughout the world. The extensive literature review in the field revealed that many papers state the invention/implementation of the method that shows great results and surpasses many others but only a few of them provide the comparison of the methods with actual tests performed. Moreover, even the publications which involve quantitative comparisons usually include 2–3 methods only.

Fortunately, in 2017 Florian Lieb, Hans-Georg Stark and Christiane Thielemann published an article with the quantitative comparison of the most recently proposed methods of spike detection. The publication describes several modern spike detection algorithms as well as introduces two new advanced techniques. The performance assessment of the proposed approaches is performed with two synthetic data sets, which imitate real raw MEA signal: the HAB data set with the sampling frequency of 10 kHz and the University of Leicester data set with the sampling rate of 24 kHz [31]. The review includes the following methods: the absolute amplitude thresholding (ABS), Precision Timing Spike Detection (PTSD) [54], Stationary Wavelet Transform (SWT) [49], Multiresolution Teager Energy Operator (MTEO) [53], Wavelet-based Teager Energy Operator (WTEO) [38], Hybrid Blind Beamforming algorithm (HBBSD) [55] and two novel techniques suggested by the authors: Time-frequency-based convolution spike detection (TIFCO) and Stationary Wavelet Transform-based Teager Energy Operator (SWTTEO). Out of 8 methods, 7 are included in the Spike Detection Toolbox MATLAB package assembled by the authors, which provides synthetic data generation script (HAB data set) as well as the environment for algorithm performance comparison.

The HBBSD and TIFCO algorithms were excluded from the current thesis on the grounds of the designated reasons. The code for the HBBSD is neither available via the link stated in the corresponding article anymore nor included into the testing environment mentioned above. Among the two newly proposed methods, the TIFCO and the SWTTEO, the authors have given the priority to the latter one for the processing of real MEA data in the subsequent publication [56], though both novel

techniques showed superior performance in the tests [31]. The six rest spike detection methods are briefly described below.

Absolute Thresholding

The absolute amplitude thresholding algorithm (ABS) involves the computation of the absolute value of the signal which is subsequently thresholded. This is the most prevalent and the simplest spike detection approach. The threshold is usually calculated based on some signal statistics such as the estimation of the noise standard deviation [43]. The algorithm is very sensitive to the noise [31], thus its performance in low SNR conditions deteriorates. The threshold value is the main parameter to adjust. This approach is identical to the old spike detection method of the research group.

Precision Timing Spike Detection

The Precision Timing Spike Detection (PTSD) algorithm was published by Maccione and colleagues in 2009 [54]. It compares the difference between the local maximum and minimum of the signal in some predefined time window and if this peak-to-peak amplitude goes beyond some threshold, the spike is assigned to the location in the signal. The time window for the detection is denoted as a peak lifetime period by authors.

The Spike Detection Differential Threshold (SDDT) is calculated by multiplying the signal standard deviation with a certain threshold calculation factor (TCF). Besides the peak lifetime period and the TCF, an important parameter for this algorithm is the refractory period: the time gap after the successful detection where no more spikes can be detected [54].

Stationary Wavelet Transform algorithm

The Stationary Wavelet Transform (SWT) -based spike detection technique was introduced by Vahid Shalchyan, Winnie Jensen and Dario Farina in 2012. The method utilizes the wavelet detail coefficients denoising with median absolute deviation (MAD) -based thresholding of each subband. The idea is that the decomposition with the mother wavelet that resembles the spike shape ought to result in the signal energy being localized in a few coefficients and the noise being spread over several coefficients. The thresholding is believed to remove the low-energy time-scale points in all scales.

At first, the decomposition of the signal over five scales of the mother wavelet is performed. Then each sub-band is thresholded with the hard threshold. The threshold calculation is based on the estimation of noise standard deviation among the obtained wavelet coefficients. It is achieved with the MAD. The obtained value is multiplied with the factor of $\sqrt{2 \log N}$, where N is the number of time samples in the signal.

After thresholding the three out of five sub-bands that contain the most of the signal energy are selected and their absolute values are summed. The result is smoothed with the Bartlett window (which length is defined as half of the putative

action potential duration) and then it is ready for the spike extraction [49]. The processing flow of the method is depicted in Figure 9.

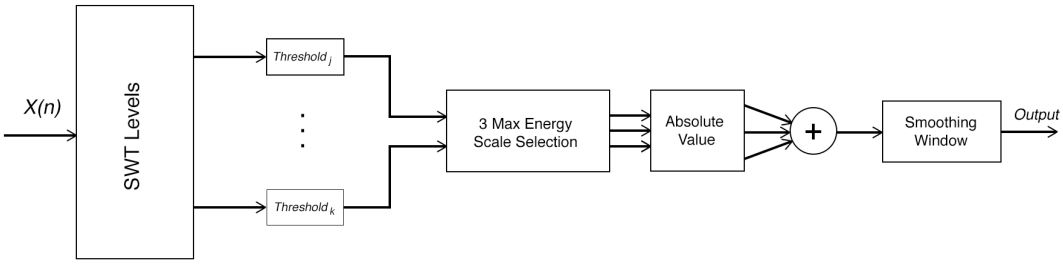

Figure 9: A block diagram of the SWT-based technique suggested by Shalchyan and colleagues (2012). Modified from [49].

Multiresolution Teager Energy Operator

The Multiresolution Teager Energy Operator (MTEO) algorithm was published by Choi and Kim in 2002. It extended the concept of the Teager Energy Operator by making it adjustable to the frequency of the action potentials. The new equation is presented below:

$$\Psi\{x(n)\} = x^2(n) - x(n-k)x(n+k), \tag{8}$$

where $x(n)$ is the input waveform and k is the resolution parameter.

As there is no a priori knowledge of the width of spikes embedded in the MEA recording, there is no insight about optimal k value as well. To get through this constrain the authors suggested using different k values simultaneously. Particularly, in the more recent paper published in 2006, it has been shown by the authors, that k values of 1, 3 and 5 yield reasonable results. The smoothing of each TEO output is implemented with the optimal window which is determined by authors to be the Hamming window of length $4k+1$. Then a maximum filter picks the maximum value for every discrete time instance from the tree smoothed TEO outputs [39, 53]. The maximum filter output is finally thresholded. Figure 10 shows the block diagram of the algorithm.

Wavelet-based Teager Energy Operator

The Wavelet-based Teager Energy Operator (WTEO) algorithm was introduced by Nabar and Rajgopal in 2009. The method comprises multi-level low-pass filtering using the father wavelet with the subsequent application of the TEO to the obtained approximation coefficients. The technique follows the classical DWT scheme with the downsamplers after each filter.

At first, a signal is decomposed into N levels by the low-pass DWT. Then the coefficients of each approximation sub-band are fed into the TEO. The TEO output is thresholded with the standard deviation-based threshold and each sub-band is

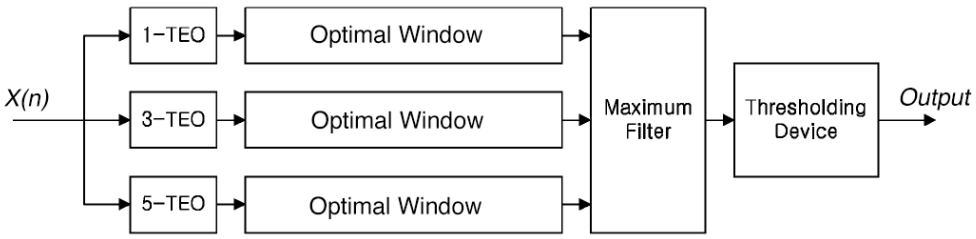

Figure 10: The MTEO spike detection method. Modified from [39, 53]

expanded to match the input signal length by zero padding. Then they are combined. The optimal TCF value depends on the level of decomposition and is defined by the user. The number of the levels of decomposition and the wavelet function selection are the main parameters of this method [38]. The block diagram of the WTEO is presented in Figure 11.

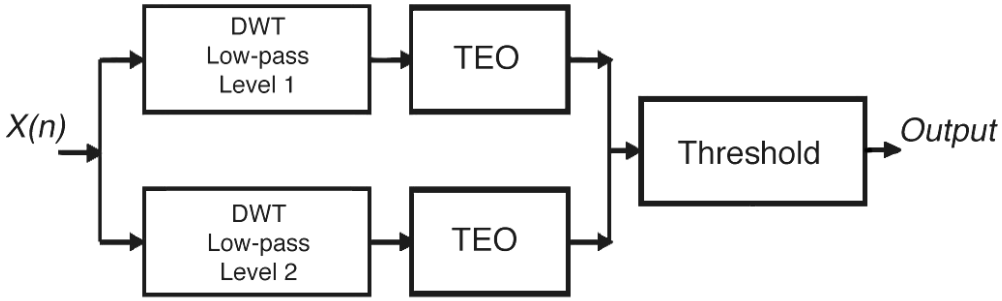

Figure 11: The Wavelet-based TEO (WTEO) method proposed by Nabar and Rajgopal in 2009. Modified from [38]

Stationary Wavelet Transform-based Teager Energy Operator

The Stationary Wavelet Transform-based Teager Energy Operator (SWTTEO) spike detection algorithm was introduced by Florian Lieb, Hans-Georg Stark and Christiane Thielemann in 2017 [31]. It is constructed as a synergy of two techniques: at first, low-pass filtering with stationary wavelet transform sub-bands is performed and the TEO is then applied to each sub-band. After that each sub-band is convolved with the smoothing window independently, the results are summed and finally thresholded.

The final sum is thresholded with the threshold that is calculated based on the noise estimation among the wavelet coefficients. It is performed via MAD-based estimation. The obtained estimation is multiplied by the TCF denoted by the authors as the "global factor". After the thresholding the spikes are extracted.

This method is the further development of the WTEO algorithm from Nabar and Rajgopal (2009) [38]. From the DWT it switches to the SWT which does not suffer from the lack of translation invariance. Thus, no downsampling of the wavelet approximation coefficients is performing, canceling the need to expand decimated coefficients at the end [31]. The block diagram of the SWTTEO method is shown in Figure 12.

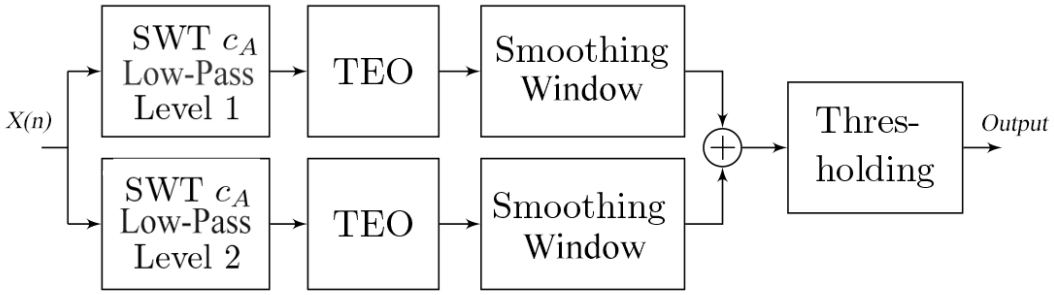

Figure 12: The SWTTEO spike detection method proposed by Lieb and colleagues in 2017. Modified from [31].

Threshold parameterization remarks

Despite the internal specifics of each described technique, these algorithms can be generalized as a two-step procedure. At first, the raw signal is converted into an indicator signal. This operation is individual for the corresponding algorithm, it could be either a simple calculation of the absolute value of the signal or a complex multi-level wavelet decomposition with an energy operator applied to its result. This step is not sensitive to the noise in the signal in terms of its implementation [31]. Subsequently, the obtained indicator signal is thresholded but the appropriate threshold value is affected by the noise a lot. Due to the difference in spiking intensity and SNR among the electrodes even within the same well of the MEA plate, it is difficult to tune the algorithm to suit all the electrodes together. The optimal multiplying factor for the threshold calculation may vary substantially from one electrode to another. Moreover, compromising parameters which would be more or less suitable for the whole plate may be not efficient. It should be denoted that this parametrization problem concerns all the algorithms mentioned above.

The authors of the SWTTEO created two versions of the algorithm. It has an autonomous mode described above when it works without any other methods involved. Another option of the SWTTEO implies the application of the algorithm together with the conventional absolute thresholding method so that the SWTTEO acts like false positive remover. Exactly this version was implemented on real data. This way it allows to drop the threshold (for absolute value thresholding) to a certain

extent and to perform full detection including the final spike extraction. The number of the detected spikes is fed into the second mode of the SWTTEO and it detects the same number of spikes. Finally, only those events that appear in both lists (within some short error time window) are considered to be true positives. The realization of this approach is described in the recent publication by Mayer and colleagues (2018) [56]. Such an implementation manner when the algorithm extracts the predefined spike number is typical for synthetic data tests as there exists the prior knowledge of the embedded action potential counts. It is not very straightforward but it allows to avoid the final threshold parametrization for the SWTTEO. When the spike number to extract is accessible there is no need to rely on any threshold value, it is possible to extract N maxima from the indicator signal, of course discarding each detected spike surroundings from it every time to avoid double capturing of the same event. This technique is further explained in Section 4.2.2 of the current thesis.

2.8.3 Algorithm performance assessment

Real MEA data can not serve as a relevant resource for the evaluation of the spike detection algorithms. The reason is that there is no any ground truth information about actual spike positions in the recordings. This fact creates plentiful complications for adequate algorithm performance assessment [31, 57].

Though visual inspection is an applicable option, it is biased and inappropriate for reliable evaluation, the maximum attainable result of such judgment is an inexact estimate of the algorithm efficiency. However, it is still performed as a supplementary quality check for the spike detection techniques [39, 49].

To overcome this constraint the simulated MEA signals with know precise spike locations and spike counts are utilized. The algorithms are fed with the generated synthetic waveform and their results are then collected. For visual assessment of the detection performance the receiver operating characteristic (ROC) curves are used. The ROC curve approaching the top and left boundary of the plot corresponds to a good performance of a method [39].

2.8.4 Synthetic Data Generation

There are many schemes for synthetic data production. But this process may be generalized as explained below. The main aim of the generation process is to create realistic synthetic signals imitating the signal from a bunch of neurons located in close proximity to the recording electrode as well as the interference from more distant neurons and the noise [57].

At first, spike templates are obtained [39]. The extraction of putative EAPs from the real recordings may be executed either visually or via statistical procedures [55]. The spike templates may be constructed from individual spikes or averaged over some collected shapes [58]. Spike amplitudes may be scaled in different ways to mimic their assumed distance variability from the electrode as well as spike polarities may be modulated [31, 59]. There exists an approach of modeling of the spikes separately at different levels of proximity to the electrode: close zone spikes are simulated as single-unit activities, more distant ones are simulated as multi-unit activities and

far spikes are considered to generate the background noise [59]. As the templates are prepared the spike trains are synthesized as Poisson's or Gaussian processes [38, 60]. The mean interspike interval and the degree of randomness of these spikes may be set to be adjustable parameters [60]. The additional distant transients may be produced as correlated or uncorrelated events [60].

For the background noise generation it is important to consider that MEAs suffer from the correlated noise. Hence, a simple addition of white Gaussian noise will not provide sufficient quality of the synthetic data and might lead to overestimation of the detection performance and biased results [38]. So-called internal noise is correlated noise as it represents the interference from the electric activity of the distant cells [39]. This noise has overlapping or even similar power spectrum with EAPs [38–40]. To simulate this noise autoregressive (AR) or autoregressive–moving-average (ARMA) models are applied. The models are obtained from real data [38–40, 58, 61]. As the noise and the spiking activity share the same spectral range, the recordings cleaned from spikes [38], noisy segments [40] or raw data chunks [49] are used for derivation of model coefficients. As an example, Yule–Walker method may be used for coefficient calculation [40, 58]. The achieved model is exploited by feeding white Gaussian noise to the derived kernel [61]. The result is the colored Gaussian noise. To imitate external noise such as thermal noise and amplifier noise some white Gaussian noise may be added [57].

In the final stage the spike trains and the noise are mixed to the aimed SNR [39]. But even such deliberate models can not fully describe the many-sided nature of the MEA signal [39], so the synthetic data still should be considered with a certain amount of scepticism.

3 Environment

The MEA recording environment was Maestro system by Axion Biosystems, Atlanta, GA, USA. The recording headstage of the system is depicted in Figure 13b. The sampling frequency of the system was 12.5 kHz. The MEA plate model was Axion CytoView MEA 48 White with 48 transparent bottom wells and 16 recording electrodes per each well. The electrode material was conductive polymer poly(3,4-ethylenedioxythiophene) (PEDOT). The six well rows were labeled by letters A–F and the eight well columns were marked by digits 1–8 as one can observe in Figure 13a. The electrode labeling in each well was composed of two digits: the first demonstrated the electrode row, the second – the electrode column. The operational software was AxIS by Axion.

(a) (b)

Figure 13: (a) Axion Cytoview MEA plate with well labeling symbols superimposed. (b) Axion Maestro headstage. The gas chamber (cap) and additional hardware of Maestro system are not shown in the picture. The figures changed from [62].

The custom data processing code of the research group, as well as new methods testing and implementation and other coding activities, were performed in MATLAB releases 2018b and 2019a by The MathWorks, Inc. under academic license.

There were two microscopes for neuronal culture examinations:

1. Microscope: Nikon Eclipse Ti
   - camera: Nikon digital sight DS-Fi2
   - software: NIS-Elements F 4.30.00 64-bit
2. Microscope: Zeiss Axio Observer.A1
   - camera: Axiocam 506 color
   - objective: 10x/0.3 Ph1 EC Plan-NEOFLUAR
   - software: With ZEN 2 (blue edition) Acquisition

4 Research methods

4.1 Cells

4.1.1 Culturing of human embryonic stem cells

Human embryonic stem cells (hESCs) were involved in the present study. The hESC line Regea 08/023 (feeder-free passages 6–8) were used. The cells were derived at BioMediTech, Tampere University, Finland. BioMediTech has approval from the Finnish Medicines Agency (FIMEA) for research utilizing human embryos (Dnro 1426/32/300/05) and supportive statements from the regional ethics committee of Pirkanmaa Hospital District for the derivation, culturing and differentiation of hESCs (R05116). The hPSC lines 08/023 were described previously by Skottman (2010) [63]. The cell lines were cultured in accordance with the publication by Rajala and colleagues (2007) [64]. Before neural differentiation the cells were transferred and expanded in feeder-free culture following Hongisto and colleagues (2017) [65].

4.1.2 Neural induction

The differentiation of neurons from hESCs was performed according to the protocol customized from Shi and colleagues (2012) [66]. For differentiation and further culturing the neural maintenance medium (NMM) was used with the composition characterized as follows: 1:1 DMEM/F12 with Glutamax and Neurobasal, 0.5% N2, 1% B27 with Retinoic Acid, 0.5 mM GlutaMAX, 0.5% NEEA, 50 mM 2-mercaptoethanol (Thermo Fisher Scientific), 2.5 µg/ml Insulin (Sigma Aldrich) and 0.1% penicillin/streptomycin (Thermo Fisher Scientific). Cultures were passaged with Accutase (Thermo Fisher Scientific) and plated onto 100 µg/ml poly-L-ornithine (PO, Sigma Aldrich) and 15 µg/ml human recombinant laminin (LN521, Biolamina) coated plates in the medium with added 10 µM ROCK inhibitor (Sigma Aldrich), which blocks the apoptosis. During the first 12 days the medium was additionally supplied with 100 nM LDN193189 and 10 µM SB431542 (both from Sigma Aldrich) with everyday medium changes (and additional culture splitting on the last day). Then during the 13th day of culturing the neural proliferation was induced by supplementing the NMM with 20 ng/ml fibroblast growth factor-2 (FGF-2) (R&D Systems).

After the 26th day, the final maturation phase began. The cell development was performed in NMM supplemented with 10 mg/ml glial-derived neurotrophic factor (GDNF, R&D Systems), 20 ng/ml brain-derived neurotrophic factor (BDNF, R&D Systems), 500 µM dibutyryl-cyclic adenosine monophosphate (db-cAMP, Sigma Aldrich) and 200 µM ascorbic acid (AA, Sigma Aldrich). Finally, on day 32 the cells were plated on transparent plastic wells with glass cover slips in their bottoms and microelectrode array (MEA) plates. Cover slips in the plastic wells were coated with poly-L-ornithine (PO, Sigma Aldrich) and 15 µg/ml human recombinant laminin (LN521, Biolamina) or mouse laminin. MEAs – with 0.1% poly-ethylene-imide (PEI, Sigma Aldrich) and 50 µg/ml human recombinant laminin (LN521, Biolamina). The cell plating densities were 50.000 cells/cm^2 for plastic wells and $1 \cdot 10^6$ cells/cm^2 for

MEAs.

4.1.3 Culturing of derived neurons

During the whole period of culturing the derived neuronal populations (both MEA and plastic well-plated) were held in an incubator at the temperature of 37 °C and humidity level 95% in 5% CO2 atmosphere. The medium solution consisted of NMM supplemented with 10 mg/ml glial-derived neurotrophic factor (GDNF, R&D Systems), 20 ng/ml brain-derived neurotrophic factor (BDNF, R&D Systems), 500 µM dibutyryl-cyclic adenosine monophosphate (db-cAMP, Sigma Aldrich) and 200 µM ascorbic acid (AA, Sigma Aldrich). The change of medium was implemented every 2–3 days. The cell extraction from the incubator for MEA recording and microscope examination was limited by 20 minutes. The MEA recordings were performed twice a week, every 3–4 days under controlled 37 °C temperature and in 5% CO2 atmosphere. The duration of each recording was 10 minutes.

4.2 Spike detection

4.2.1 Default algorithm

The old spike detection method constitutes the thresholding with the band-pass prefiltering. The raw data are first prefiltered with the fourth-order band-pass elliptic filter with a lower passband frequency of 200 Hz and a higher passband frequency of 3000 Hz.

The threshold is calculated by multiplying the estimate of the background noise standard deviation with certain TCF. The standard deviation of the noise was estimated by taking the median of the absolute signal divided by 0.6745 constant [43]. In the research group different values of the threshold calculation factor are used for data acquired with Axion and Multichannel Systems recording environments. These values are 6 and 5 correspondingly. The difference is based on empirical experience over the years of working with these two systems. The samples of the prefiltered signal that exceed the calculated threshold are thought to belong to action potentials. The time stamps of the spikes are obtained by extraction of the local maxima of the segments of the signal above the threshold.

The time when the next spike can not be detected after the captured event is set to approximately 0.7 milliseconds. Supposedly, this interval is shorter than the usual refractory period for a neuron but it is set to such a small value because there are many neurons in the proximity of the detecting electrode. Hence, there is a probability of the presence of more than one dominant spike train captured by the electrode [67]. In the final stage of the spike detection procedure, the spikes exceeding another threshold calculated from the estimate of the noise standard deviation with the TCF of 50 are erased from the spike list. Such spikes are considered as artifacts. For example, it was noticed that some Axion recordings contain several hundreds of samples with enormously large amplitude in the end. The voltage values of these samples can not be produced by any biological phenomena occurred among the cell population.

4.2.2 New algorithm selection

The SWTTEO was selected as a priority candidate for the new algorithm for the research group based on the superior results demonstrated in the synthetic data tests [31] and as it was tested on real MEA data [56]. To confirm the efficiency of the method it was decided to replicate the evaluation procedure implemented by Lieb and colleagues (2017) in the corresponding publication as the above mentioned Spike Detection Toolbox was publicly available online. The six algorithms described above were tested with the HAB data set available in the package.

Replication of Simulations

The MATLAB environment Spike Detection Toolbox provided by Lieb and colleagues (2017) included the absolute amplitude thresholding algorithm which was similar to the default algorithm of the research group. The main goal was to confirm the superiority of the SWTTEO method over the conventional absolute amplitude thresholding. Also, the evidence of its advantage over other algorithms involved in the tests was appreciated.

The toolbox even had an option for prefiltering of the data with the band-pass filter before the application of the algorithms. The suggested filter was replaced by the default elliptic filter. The default filter was chosen to be involved in the future work instead of the suggested one due to computational speed considerations. These two filters (the default one and the one proposed by Lieb and colleagues (2017) [31]) had roughly similar frequency responses. In the arranged correspondence the authors claimed that in accordance with their research the raw data prefiltering would not critically affect the SWTTEO detection performance. The prefiltering was involved not only in the replications of tests but also in real data processing as the performance of the absolute amplitude-based thresholding algorithm (which is needed for real data application version of the SWTTEO) depends on it.

Parameters for the six algorithms

The codes of all the algorithms were comprehensively studied. The optimal parameters for the algorithms were selected based on the information provided in the original publications with the data-specific adjustments recommended by Lieb and colleagues (2017). Of course, optimality criteria should be considered with some criticism, as the algorithms were optimally tuned by authors on dissimilar data sets, hence for the different data the actual optimal parameters may differ from those stated by the developers.

Symlet5 wavelet family was selected for all wavelet-based methods as the trials by Lieb and colleagues (2017) confirmed its optimality for the data. The selection of the decomposition level was based on the sampling frequency which was 10 kHz for the HAB data set.

The parameters for the PTSD algorithm included a peak lifetime period which was set to 0.5 ms and a refractory period which was selected to be 1.2 ms.

For the WTEO the 2 levels of decomposition were chosen. It was proven by Nabar and colleagues (2009) that it is sufficient even for the data with the sampling rate of 20 kHz [38].

The SWT requires the decomposition level as well. It was set to 5, as it had been proposed by its authors in the corresponding article [49].

The optimal parameters for the SWTTEO algorithm were set as it was explained in the article. The length of the smoothing window was selected to be 1.3 ms and the decomposition level of 2 was chosen.

The last parameter for all these four algorithms and the only parameter to tune for the ABS and the MTEO algorithms was the threshold value for the obtained indicator signal. But as it was mentioned above it is not required in case of the spike extraction with the predefined spike number. The number of action potentials had been preset during the synthetic data generation and thereby this value was used in the last step of each algorithm implementation. The spike extractor finds the maximum in the indicator signal. The timing is then written in the spike list and the surrounding region of this maximum is zeroed (cleared) within the defined window to fully remove the detected event from the signal and to avoid double detection of the same transient. Afterwards, the extractor moves to the next maximum in the indicator signal. The procedure is iterated until the required spike number is reached. This approach escapes any errors due to improper threshold tuning.

There are a few remarks about the arrangement of the testing environment. First of all, in the paper on the WTEO algorithm each sub-band was thresholded separately [38] while in the code by Lieb and colleagues (2017) the sub-bands were summed and then thresholded. Presumably, it is done to minimize the difference between the WTEO and SWTTEO approaches and to adapt the WTEO to the testing procedure. Moreover, Lieb and colleagues (2017) claimed that the WTEO performed poorly because it lacks a smoothing window after the TEO step that would optimize its behavior [31].

Synthetic data generation

The aim was to generate a signal with known spike timings which would closely imitate the real MEA recording. The generation procedure was based on that presented in the Spike Detection Toolbox by Lieb and colleagues (2017) [31] with the inserted prefiltering to achieve the similarity of the ABS algorithm with the absolute amplitude thresholding method that was in use in the research group and to confirm the SWTTEO performance on the prefiltered data.

The signal was assembled as a linear sum of scaled spike templates and modeled noise. The three spike templates provided by Lieb and colleagues (2017) were extracted from 10 kHz MEA recordings of hESCs-derived three-dimensional neurospheres which were plated on MEA wells 24 hours before the recording [31]. These templates differed in their shape and polarity. The main assumption of the model was that there existed only a few cells nearby the electrode whose activity was possible to discern in the noise. The amplitudes of randomly chosen spike templates were scaled with the distance factor $\xi < 1$. The randomly chosen time point τ of each

inserted spike was selected so that there was no overlap among the transients. The insertion process was repeated until the selected number of spikes M was achieved. The background noise was simulated by AR(551) model which was derived from the same MEA data. The Gaussian noise was used as an input for the AR model. The noise amplitude was modulated by a parameter σ. The mentioned spike templates and the 551-element noise filter were provided in the package. Equation 9 represents the described data generation process.

$$s(t) = \sum_{k=1}^{M} \xi_i \psi_i(t - \tau(k)) + \sigma n(t), \tag{9}$$

where $s(t)$ denotes the generated signal, ξ_i expresses the scaling factor, ψ_i expresses the i_{th} inserted spike, $\tau(k)$ shows the random timing for the insertion, $n(t)$ represents the background noise and σ – its modulation parameter.

The data sets of 60000 samples length were generated. The sampling frequency was set to 10 kHz and the spike count was fixed to 100. Hence, each generation resulted in 6 second signal with 100 spikes embedded. The two SNR values were chosen to represent the high and low SNR conditions: 4.63 and 2.07 correspondingly. The tests were performed on raw and prefiltered signal.

Performance measure

The performed synthetic data simulations were evaluated by building the ROC curves. Though in both publications by Lieb and colleagues (2017) [31] and also by Choi and Kim (2002) [53] the horizontal axis of the ROC curve was labelled as representing False Positive Rate (FPR), it was obvious that the canonical calculation formula for this metrics did not suit for evaluation of action potential detectors because it included True Negatives (TN) value in its denominator. Due to the fact that the spike detection algorithms do not constitute the classical binary classifiers, it is problematic to follow the actual formula for the FPR. For example, the idea of considering each sample that is not selected as a spike position by an algorithm as the TN will produce the FPR values that are not representative because there is an extremely larger number of samples in MEA recordings that are not related to distinguishable action potentials. Moreover, the algorithms select only one sample to indicate the timing of each action potential though many samples are involved in the segment that depicts the EAP in the recording. The authors rather used the ratio of False Positives (FP) to the total count of spikes embedded into the synthetic signal to calculate the FPR*. That is why the FPR* is marked with a star sign "*". In the current work the same technique was used for the FPR* calculation. The obtained ROC curves were cut when the FPR* achieved 40%.

The simulation code provided by Lieb and colleagues (2017) [31] sets the FPR* value fixed from 1 to 40 and self-adjust the number of events for the algorithm to extract to fit this value. As the required FPR* value is achieved the code calculates the corresponding TPR value based on the extracted events. The results of the TPR have been averaged over 20 trials for each fixed FPR* value. Each trial is accomplished with a unique newly generated signal. The obtained 40 TPR values

(that correspond to the FPR* values from 1 to 40) comprise the ROC curve. The procedure is iterated for each of the six algorithms.

4.2.3 Selected method parameters for real data

The validated SWTTEO algorithm required parametrization before extensive application on real data. As the algorithm is implemented on real MEA data by its authors and in the presence of the confirmed advantage of the method the aim was finally to incorporate it into the MEA signal processing network of the research group.

It is important to recap that the mode of the algorithm which was suitable for the real data applications involved the conventional absolute amplitude thresholding (lowered threshold) with the subsequent removal of putative false positives with the SWTTEO.

As it has been stated previously, the algorithm has three main parameters to be set: the wavelet type, the decomposition level and the smoothing window length. The authors assert that the parameters for the SWTTEO algorithm can be selected based on the sampling frequency and the average spike duration only [31].

The SWTTEO parameters for real MEA data processing had to be re-examined due to the difference between the synthetic data and the real signal. Though specific distinctions were obviously not available the main point to consider was the sampling frequency dissimilarity: the real signal was sampled with the sampling rate 12 500 Hz for Axion MEA and 25 000 Hz for Multichannel Systems MEA, while the HAB synthetic data set had the sampling frequency of 10 000 Hz.

As it has been mentioned previously the level of the wavelet decomposition depends on the sampling rate. The spike-specific frequencies should be covered. The range approximately from 300 Hz up to 3000–3500 Hz is considered as the spike-specific (which means that most of the desirable electrical activity should fall within this band). As a compromise between two sampling frequencies, the decomposition level of 3 was selected. The coverage of the decomposition levels is organized as described below.

In the first case (sampling frequency 12 500 Hz): 1st level coverage is from 0 to 6250 Hz, 2nd – from 0 to 3125 Hz and 3rd – from 0 to 1563 Hz. In the second case (sampling frequency 25 000 Hz): 1st level covers frequencies from 0 to 12 500 Hz, 2nd – from 0 to 6250 Hz, 3rd – from 0 to 3125 Hz. To enhance the capturing in the low-frequency domain, the 4th level of decomposition could be involved in the second case for the band from 0 to 1563 Hz. However, the lower part of the spike-specific frequency band is sometimes superpositioned with the 1/f noise as it has been mentioned in Section 2.7.3 that is why this option worth some critical consideration.

The smoothing window length was selected based on the discussion with the biologists about the spike lengths. According to Lieb and colleagues (2017), some variation in this parameter is acceptable. It has been concluded that spike duration is around 0.5–1 ms or a bit more which is similar to the stated in the article [31], so the default window length of 1.3 ms suggested by the authors has been selected.

The selection of the wavelet type was as well performed based on the recommendations of the authors. As it was mentioned above the authors tested the algorithm

with two synthetic data sets and it was found that the Symlet5 wavelet family (father wavelet in this case) had shown the best results [31].

The important parameter to select was the threshold calculation factor for the absolute amplitude thresholding algorithm because different values led to different numbers to be fed to the SWTTEO (and different counts of prospective false positives for it to cancel). Two experienced biologists visually analyzed the performance of the algorithm in different conditions. The data generated by the rat cells and hESCs-derived neurons in different maturation stages and under various medical treatments were tested with the TCFs 3.5, 4 and 4.5. Each detection was performed on a single electrode recording extracted from a 16-electrode well recording. During excessive visual inspection of the detection results, the determining factor became the detection of the spiking activity under tetrodotoxin (TTX) treatment. TTX is a potent toxin that binds to voltage-gated sodium channels and inactivates them thus making the occurrence of any action potentials impossible. For reader's considerations here should be stated that the detailed examination of some single electrode 10 minutes TTX recordings has revealed that several tens of putative action potentials still may happen even under TTX treatment. In reality, some occasional events still happen among the cell population but the numbers are obviously less than in case of normal spontaneous activity. Both biologists agreed that the thresholding factor 4.5 is the best as it resulted in the acceptable number of implied spikes in the signal recorded from cells treated with TTX. The authors selected the same value in their publication [56]. Table 1 shows the numbers of the detected spikes for different single electrode recordings extracted from full recordings. The conditions include hESCs-derived neuronal populations in two maturation stages and under pharmacological treatments with TTX, gabazine – $GABA_A$ receptor antagonist and kainic acid; there are rat cells and rat cells under gabazine treatment; at the end of the table – the recordings of rat and human cells with specific bursting patterns developed. These intermediate detection results were important for the parametrization of the algorithm. The detection results of the parametrized algorithm are discussed in Section 5.

4.3 Pharmacological experiments

The pharmacological experiments were conducted on day 44 of cell development on MEAs. From the whole plate, 8 wells with the most active networks were chosen for the pharmacological manipulations. The wells C5, E5, E6, E7, F5, F6, F7, F8 were selected. At first, the baseline activity was recorded for 10 minutes. Then the wells C5, E6, E7 and F5 were chosen to be the control group wells while the wells E5, F6, F7 and F8 were treated with kainate receptor agonist kainic acid (5 µM, Sigma). The drug application period was 255 seconds with the following 10 minutes recording of the provoked activity. Then the subsequent treatment with the voltage-gated sodium channel blocker tetrodotoxin (TTX, 1 µM, Tocris) was performed on wells E6, F5 (control group) and E5, F6 (after kainic acid treatment). The treatment interval lasted 133 seconds. The following 10 minutes were recorded again. All pharmacological agents were applied into 500 µl MEA wells in 30 µl volume with higher concentration thus resulting in the stated final concentration in 530 µl. For

Table 1: The table demonstrates the numbers of the spikes detected by the SWTTEO in conjunction with the absolute amplitude thresholding algorithm with different TCFs. The first column describes the cell types and the conditions involved. The rightmost column demonstrates the detection results of the old absolute amplitude thresholding algorithm alone with TCF 6 for these conditions. The colors represent the opinion of the biologists. The red color demonstrates potentially undesirable result, the yellowish shows questionable result and the green – reasonable result. The detections are performed on single electrode recordings of 10 minutes duration.

Condition/TCF	3,5	4	4,5	Old alg. with TCF 6
Day 39	1961	1312	992	527
Day 56	3226	2259	1675	941
Baseline	6474	5159	4071	2472
TTX	455	64	3	0
Gabazine	3098	2076	1317	468
Kainic acid	4273	3020	2231	914
Rat cells	1745	1342	1130	1089
Rat cells gabazine	2194	1635	1329	782
Rat cells block bursts	3342	2807	2529	2443
Human cells bell bursts	6309	4909	3796	2288

further data analysis only the 10 minutes segments are considered valuable. The recording intervals that contain drug addition are usually not processed because the signal may be distorted by medium shaking during its pipetting up and down.

5 Results and discussion

5.1 Neuronal development

The regular monitoring of the spontaneous electrical activity of the cell cultures during the MEA recordings as well as the immunocytochemical staining of the plastic wells with cover slips performed by laboratory staff confirmed the development of functional neural networks. The specific neuronal morphology which is characterized by the extension of neural processes was visible under the microscope. As there are sufficient cell plating density differences between the MEA wells and the plastic wells with cover slips it is more comfortable to examine the branching processes in the latter ones. During the microscope examination of the plating results there appeared also the difference in the cell density among the plastic wells. This variability is usual and happens due to manual plating procedure. Figure 14 depicts the MEA and plastic wells under the microscope.

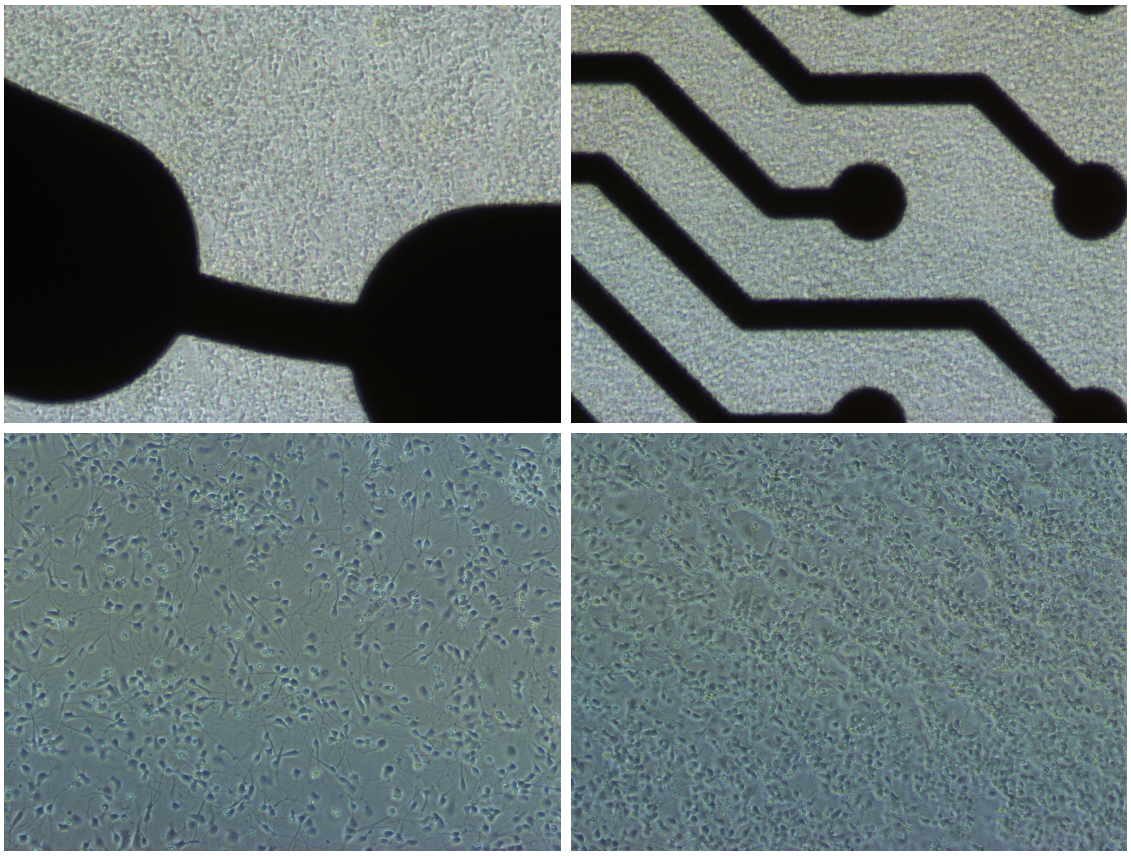

Figure 14: Upper row: cell cultures in the MEA wells. Lower row: cell cultures in the plastic wells with cover slips. It is possible to notice the cell plating density difference between the MEA and plastic wells and sufficient variability in the cell densities of the lower row wells. The photos are taken on the day in vitro 33 with Nikon Eclipse Ti microscope, 10x magnification.

Regular MEA monitoring showed that the most active networks developed in the

right lower half of the MEA plate. As it was mentioned above the wells C5, E5, E6, E7, F5, F6, F7, F8 were chosen for the pharmacological manipulations. The photos in Figure 15 show some of the selected wells on the day in vitro 53.

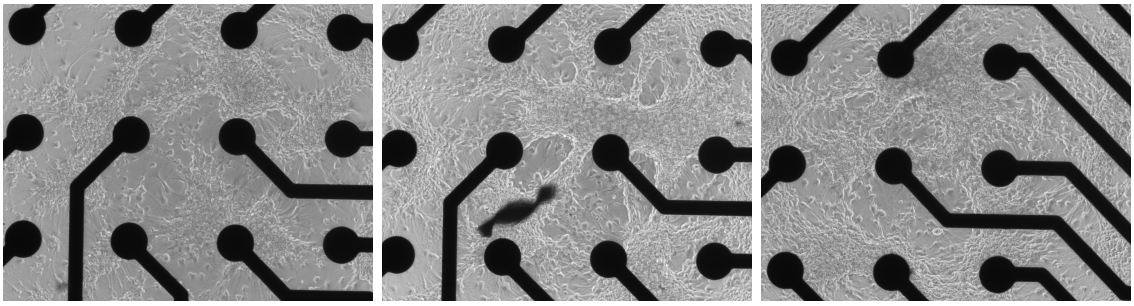

(a) E6 (b) F5 (c) F8

Figure 15: The three wells that were involved into pharmacological experiments, E6 and F5 from the control group and F8 that was subject to kainic acid treatment. The microscopic photography was performed on day in vitro 53, 22 days before the experiments. The photos are taken with Zeiss Axio Observer.A1 microscope, 10x magnification.

5.2 Receiver Operator Characteristic

The six algorithms were tested with the synthetic data under different conditions as described in Section 4.2.2 and corresponding ROC curves were constructed. Figure 16 demonstrates the resulting ROC curves.

One thing to denote is that the WTEO has been applied in a bit distorted manner as it was mentioned in Section 4.2.2. Moreover, in the article by Lieb and colleagues (2017) it was pointed out that the performance of the WTEO algorithm is weak because there is no smoothing of the Teager energy operator output and some spikes are detected twice [31]. These facts may explain why the WTEO demonstrates bad results in the present tests.

Under sufficient SNR conditions (SNR=4.6, higher row) it is possible to see that in both cases with and without prefiltering the SWTTEO dominate in the performance and the MTEO does approximately the same job as well. Their results are closer to the left upper corner of the ROC plot. The PTSD follows them and the SWT is next to it in a case without the filter. The detection performance seems to deteriorate with the prefiltering turned on. This is kind of expectable as the filtering procedure smoothes the shape of the waveform, especially it affects "distant" low amplitude spikes and the algorithms fail to capture them. In case of real data operation the prefiltering is necessary due to, for example, low-frequency fluctuations of the waveform around zero line as well as other possible undesirable noise components that occupy the frequencies that are considered non-spike-specific. While the efficiency of all other algorithms sufficiently dropped with the prefiltering the performance of the ABS algorithm (which was similar to the old method of

the research group) remained stable though it was still less than the results of the SWTTEO and MTEO under these settings.

Under low SNR conditions (SNR=2, lower row) the SWTTEO showed the best performance only in the case with enabled prefiltering while the results of the trial without it were surprising. Here it is possible to see that the PTSD algorithm demonstrated some better outcomes in the rightmost half of the ROC curve. Another point was that prefiltering did not spoil the performance of the SWTTEO and boosted the performance of the absolute amplitude thresholding under these conditions. Of course, under such low SNR the detection performance is very poor in total for all of the algorithms. Lieb and colleagues (2017) in their publication used no prefiltering and did not drop the SNR lower than 2.796. In their trials, the SWTTEO performance was superior to all the algorithms mentioned in this thesis along the whole ROC curve in all conditions regardless of the noise level [31]. However, these results confirmed the advantage of the SWTTEO algorithm. It was finally selected as the new method for the research group. Its version that suits the real data application was inserted into the custom data processing code of the research group.

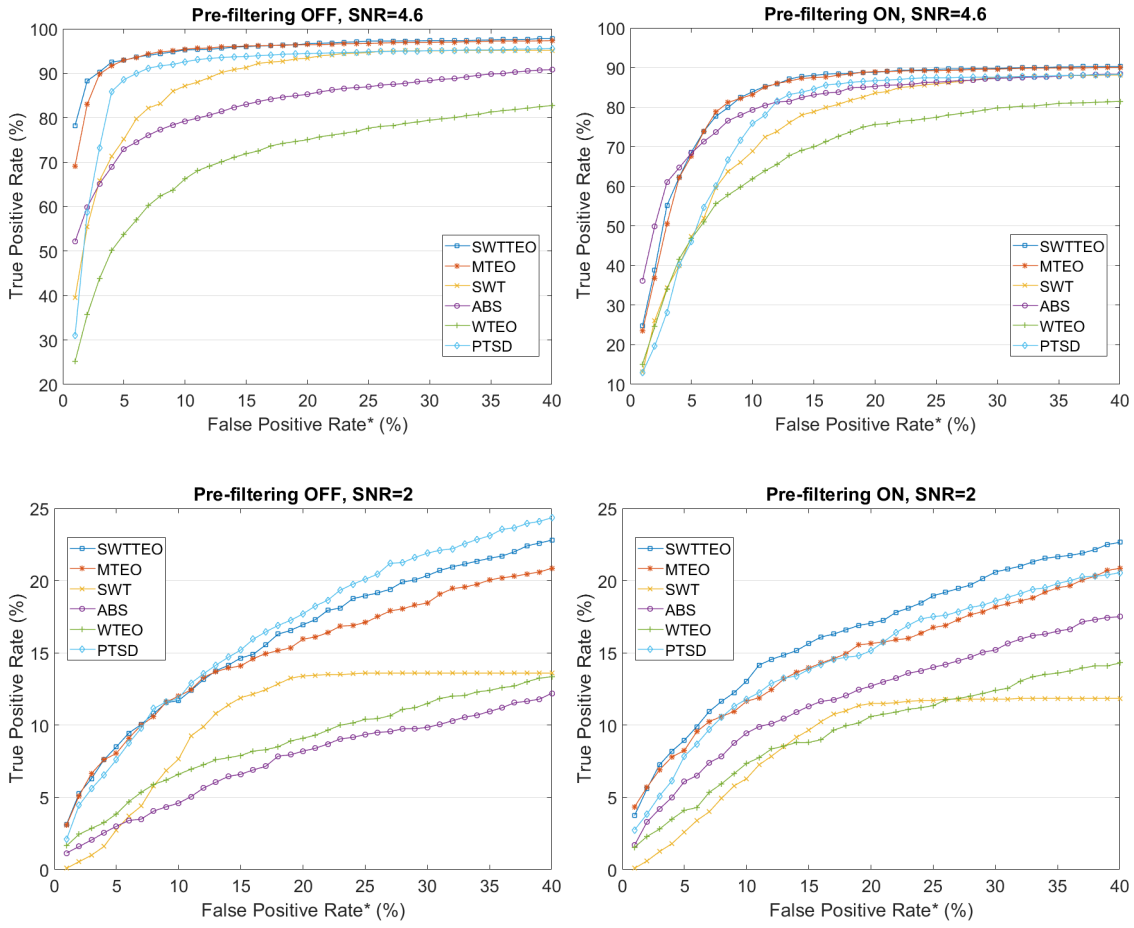

Figure 16: ROC curves under the high and low SNR with and without the prefiltering.

5.3 Raw signal

Before moving to the real data detection of the new algorithm it is crucial to visualize the difference in signal behavior under different pharmacological treatments. As an example, Figure 17 demonstrates the waveform recorded from the well F6, the electrode 34 under different conditions: baseline activity, kainic acid treatment and subsequent TTX treatment. The baseline activity contains LFP fluctuations with

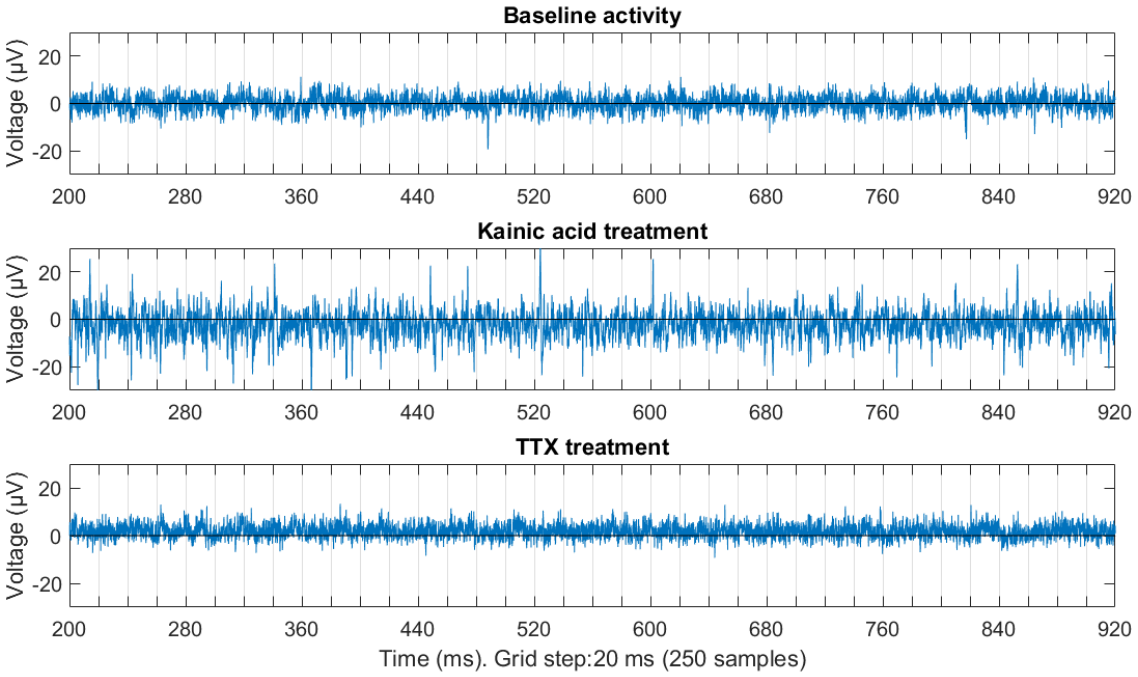

Figure 17: A raw signal under different conditions. Well F6, electrode 34.

some noticeable spiking activity. When kainic acid is added the amplitude of the LFP fluctuations rises noticeably. It is possible to distinguish some EAPs there. Finally, after the TTX treatment the spikes disappear. Some shift of the waveform above zero line is clearly visible in the TTX case. That is why the prefiltering is important.

5.4 Detection results

The numbers of the detected events and the visual detection performance assessment are the only available processing quality measures in a real data challenge. Several comparative figures are presented to indicate the growth of the detected spikes numbers with the new algorithm application. The old and new algorithms are compared to each other. Figure 18 displays a segment of the well F6, the electrode 34 signal under kainic acid treatment. The visual assessment confirms that the events captured by the algorithms seem to represent EAPs. It is possible to notice that the count of the detected spikes has increased sufficiently with the new method. The plot is arranged on a bigger scale to demonstrate longer segments of the signals.

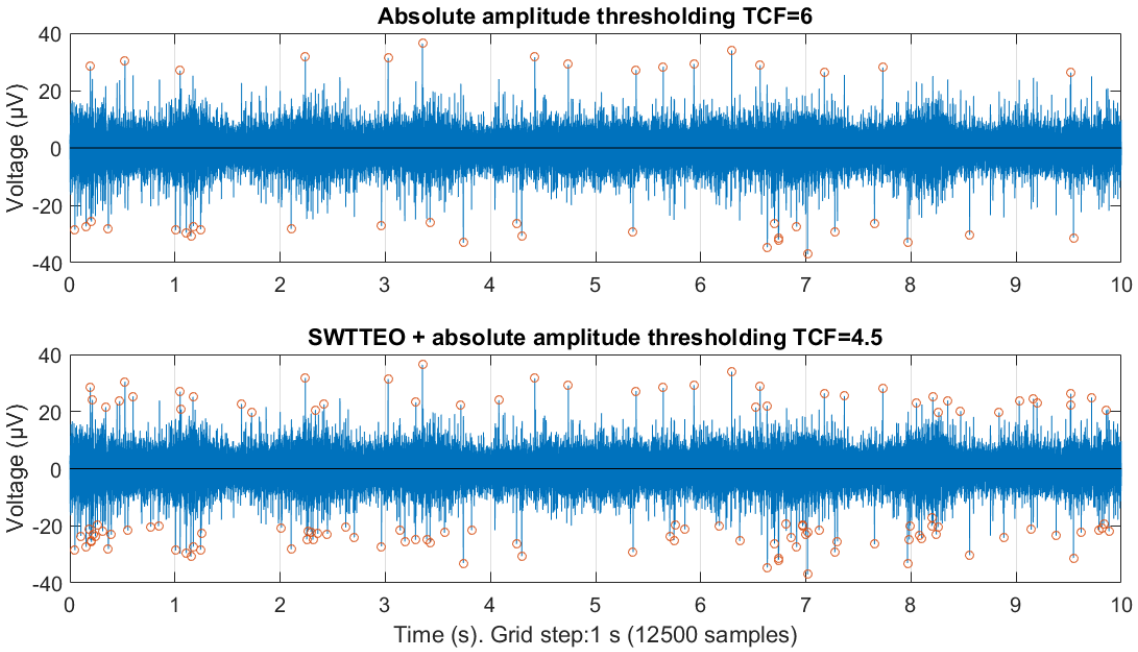

Figure 18: Well F6, electrode 34, kainic acid treatment: detection performance of the algorithms. The captured events are displayed as small red circles on top of the prefiltered signal.

To build a representative visualization of the change in the numbers of the spikes detected the well F6 with its all 16 electrodes was plotted in Figure 19. The detection for the well is shown under mentioned three pharmacological conditions. The numbers of the detected events were plotted in circles that represent the electrodes. The left side of each circle depicts the spike number caught by the new algorithm and the right one – by the old. It is clear that in all cases the new algorithm captured significantly more events. In many cases the differences exceed 50%. For better understanding, the heat map is embedded in the circles and its color bar is shown in Figure 19d.

Finally, three histograms were constructed to represent the three stages of the pharmacological experiments. The spike counts demonstrated in the histograms represent the detections per whole wells with 16 electrodes in each (that is why they should not be compared with the numbers in Table 1 or in the separate circles of Figure 19). The first histogram in Figure 20 shows the total detection numbers for the wells C5, E5, E6, E7, F5, F6, F7, F8. The detection result of the new algorithm is represented by the red bars, and the score of the old one is shown by the blue bars. Each bar has the exact detection number on top of it. The well F6 involved in the previous visualizations demonstrated the highest activity during the baseline activity recording.

As it was said the wells C5, E6, E7 and F5 were chosen to be the control group wells while the wells E5, F6, F7 and F8 were treated with kainic acid. The next histogram displayed in Figure 21 illustrates the captured events among the control

group and under kainic acid treatment (its rightmost half). Again, the new method detected more spikes than the old one in all cases. The difference in the counts exceeds 50% in some examples.

It is worth emphasizing that with the addition of the kainic acid the numbers of the captured events decreased for all the wells involved (with both algorithms) except for the well F7 where the counts increased slightly as it is visible in Figures 20 and 21. One possible explanation might be excitotoxicity that happens with kainate receptors [68]. But the examination of the waveforms, for example, in Figure 17 reveals that there is a remarkable increment in the LFP amplitude which theoretically informs about the activity growth. Hence, the reason for the lower spike counts obtained in the case of kainic acid treatment is most likely different. It may be the masking that LFP provides for EAPs. As the SWTTEO still relies on the absolute amplitude thresholding (even with the lowered threshold) the latter one may lose its performance in the case of the sufficient LFP growth. That is why the field of the algorithm development stands open. Some approach with the automatic and flexible tuning of the SWTTEO without any absolute amplitude thresholding involved if found may dominate in performance. Another evidence obtained by the biologists during synchronous network activity analysis (when all 16 electrodes of the well are examined together) which was beyond the scope of the current thesis revealed that though the local single electrode spike numbers may grow under the kainic acid treatment, the synchronous bursting activity at network level (whole well) deteriorates and the bursts recorded from the separate electrodes tended to shorten. This is another suggested reason for such results.

The last histogram is demonstrated in Figure 22. The wells E6, F5 (the control group) and E5, F6 (after the kainic acid treatment) were treated with TTX and other wells remained untouched. It is visible from the three histograms in total that the untouched wells maintained the same activity level why those four treated with TTX dropped their spiking level almost to zero: while new algorithm still detected several hundreds of spikes per whole wells, the old one did not catch anything.

5.5 Discussion on spike detection methods and prospects

The new method detects spikes better but it still extracts only the obvious outliers from the noise while the lower ones might contain the EAPs as well. Whether some lower deviated peaks should be extracted is an open-ended question. As practice shows, for some cases (with high SNR) a simple drop of the threshold value even for the old absolute amplitude thresholding algorithm alone leads to remarkably larger counts of the detected spikes and the captured events with a high probability express the actual EAPs in accordance with the visual analysis. However, if some other electrodes incorporate more noise it will result in critical numbers of false positives there. For the kainic acid treatment, the lowered threshold may ruin the operation of this algorithm leading to meaningless output. The main advantage of the new method is that it provides larger detection numbers with sustainable behavior in different conditions.

It would be a good idea to get rid of the initial absolute amplitude thresholding

part for the real data application of the SWTTEO. Nevertheless, the attempts to find the universal "global factor" for its autonomous mode that would provide accurate denoising of the coefficients for various recordings were not successful. From the arranged correspondence with the authors, it was found that they faced the same issue.

Another point is that the MTEO algorithm performs almost as well as the SWTTEO in the synthetic data tests and under sufficient parametrization it may provide similar efficiency with less computational complexity. But the MTEO requires the thresholding of its output as well, and thus it is prone to have the same problem while applied to the real data.

The principle of the PTSD is promising in terms of the searching for noise hidden voltage jumps and the experiments in the current work demonstrate that it has possible benefits in low SNR conditions. But the indicator signal thresholding issue exists here too.

For large spike detection frameworks, it may worth to utilize different algorithms for different data. As an example, for cell populations that tend to show clear activity with high SNR the application of the absolute amplitude thresholding alone is satisfactory and there is no sense to involve any complex and computationally demanding techniques: the code execution will be longer but the results will be the same. On the other hand, if the analysis switches to some noisy recording, then some advanced approaches are required. Of course, a particular cell population has to be analyzed with a single approach only during all recordings of its activity.

A useful option is to produce the signal-specific synthetic data for each particular population. It will enable precise tuning of the algorithm based on the spike shapes extracted from the actual recordings. However, for normal MEA laboratory workflow, such practice would be cumbersome. Another approach is to implement some unsupervised learning for the parameter selection and/or optimization as it has been performed in the article by Shalchyan and colleagues (2012) [49].

The noise is still a big problem. As the addition of TTX almost silences the activity of the cells, the obtained signal may be studied in detail to produce some reliable noise model. Such a model will be useful for the processing of the data recorded before the addition of TTX.

For comprehensive cell network characterization, it is possible to perform network-level synchronous EAP analysis as it has been suggested in a work by Eytan and Marom (2006) [69]. Network spikes are short synchronized events that happen in the cell population. Together with the synchronous bursting activity features, it may bring vast insight into the network activity patterns.

The advanced suggestion would be to grow a neuronal culture on top of the high resolution (HD) MEA plate which has enormously large density of the microelectrodes, and to create a connectome of the network using modern microscopy advances. Then the challenge would be to assign every single spike to a particular cell by solving the problem of signal source localization. The next step would be an attempt to build a mathematical model of the network.

The field of neuronal signal processing is expanding and new findings are appearing on the horizon.

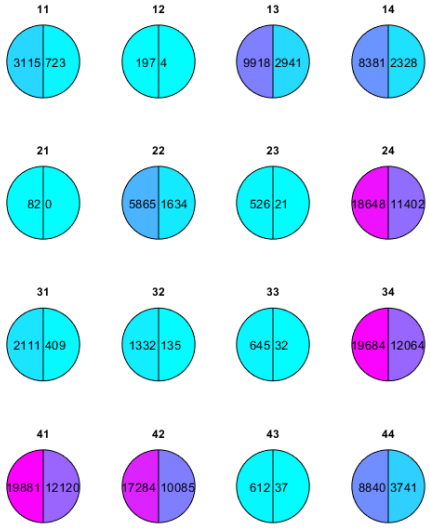

(a) a

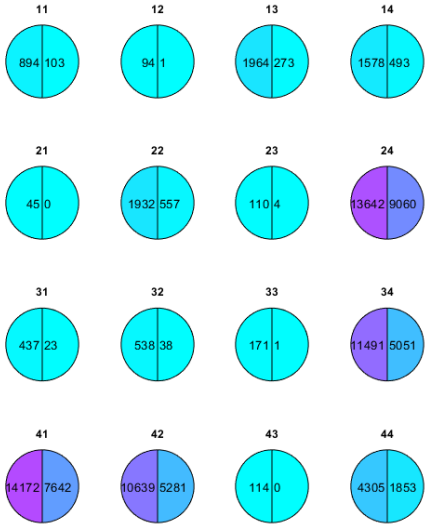

(b) b

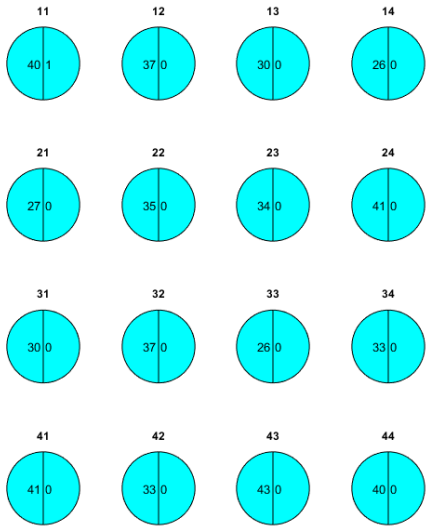

(c) c

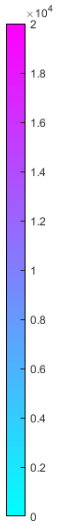

(d) d

Figure 19: The detection results of well F6 under different conditions a) Baseline b) Kainic acid c) TTX. Each circle represents the electrode with the label on top. The number from the left of the line shows the spike count detected by the new algorithm and from the right – by the old. d) A color bar for the heatmap visualizes the detected spike count.

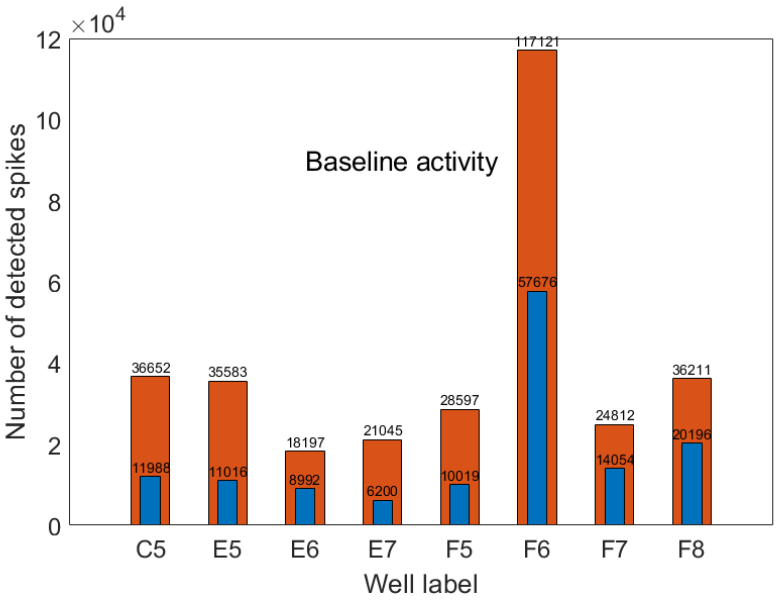

Figure 20: Baseline activity. Detection results in spike numbers per wells. The red bars demonstrate the numbers of spikes captured by the new algorithm and the score of the old one is shown by the blue bars. The wells are arranged in alphabetic order.

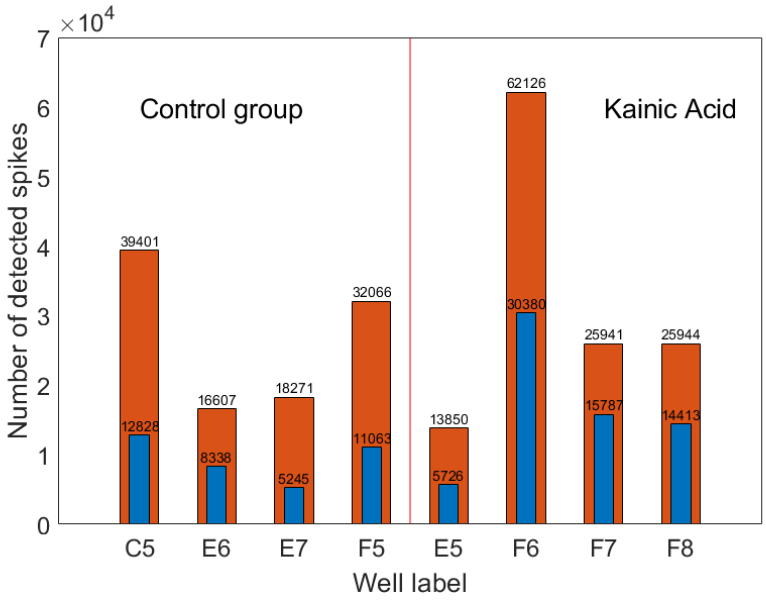

Figure 21: Kainic acid treatment. Detection results in spike numbers per wells. The red bars demonstrate the numbers of spikes captured by the new algorithm and the score of the old one is shown by the blue bars. The wells are displayed as two groups separated by a thin red line. The control group received no treatment while the other group was treated with kainic acid.

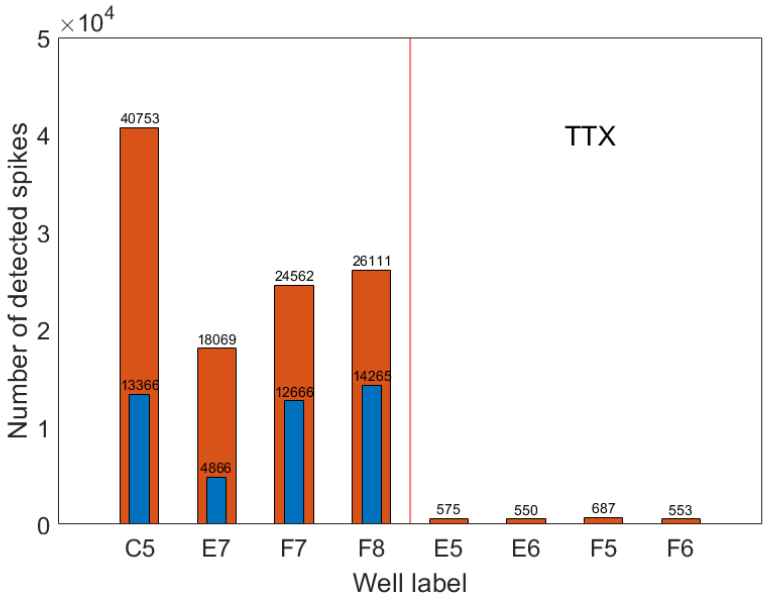

Figure 22: TTX treatment. Detection results in spike numbers per wells. The red bars demonstrate the number of spikes captured by the new algorithm and the score of the old one is shown by the blue bars. The wells at the left from the red line remained untouched while the wells at the right from it received the TTX treatment.

6 Summary

The thesis project is considered successful as the new method was tested and embedded into the research group MEA processing framework. The synthetic data tests confirmed the advantage of the approach in most conditions. Moreover, the detected spikes counts showed significant growth in real data applications. Visual examination of the detected events on top of the prefiltered data validates the improvement.

There still exists the potential for further development of the algorithm to achieve even better performance in challenging conditions.

References

[1] F. B. Mark, P. Michael, and W. C. Barry, *Neuroscience: Exploring the Brain 4th Edition*. Wolters Kluwer Health, 2015.

[2] D. Johnston and S. M. Wu, *Foundations of cellular neurophysiology*. MIT Press, 1995.

[3] J. Mertens, M. C. Marchetto, C. Bardy, and F. H. Gage, "Evaluating cell reprogramming, differentiation and conversion technologies in neuroscience", *Nature Reviews Neuroscience*, 2016. DOI: 10.1038/nrn.2016.46.

[4] I. K. Suzuki and P. Vanderhaeghen, "Is this a brain which I see before me? Modeling human neural development with pluripotent stem cells", *Development*, 2015. DOI: 10.1242/dev.120568.

[5] T. Papouin and P. Haydon, "Obtaining Acute Brain Slices", *Bio-protocol*, 2018. DOI: 10.21769/bioprotoc.2699.

[6] S. H. Cheshier, M. Y. S. Kalani, M. Lim, L. Ailles, S. L. Huhn, and I. L. Weissman, "A neurosurgeon's guide to stem cells, cancer stem cells, and brain tumor stem cells", *Neurosurgery*, 2009. DOI: 10.1227/01.NEU.0000349921.14519.2A.

[7] F. Lu and Y. Zhang, "Cell totipotency: Molecular features, induction, and maintenance", *National Science Review*, 2015. DOI: 10.1093/nsr/nwv009.

[8] K. Cockburn and J. Rossant, "Making the blastocyst: Lessons from the mouse", *Journal of Clinical Investigation*, 2010. DOI: 10.1172/JCI41229.

[9] A. Farin, C. Y. Liu, J. B. Elder, I. A. Langmoen, and M. L. Apuzzo, "The biological restoration of central nervous system architecture and function: Part 1-Foundations and historical landmarks in contemporary stem cell biology", *Neurosurgery*, 2009. DOI: 10.1227/01.NEU.0000337580.02706.DC.

[10] K. Rajala, B. Lindroos, S. M. Hussein, R. S. Lappalainen, M. Pekkanen-Mattila, J. Inzunza, B. Rozell, S. Miettinen, S. Narkilahti, E. Kerkelä, K. Aalto-Setälä, T. Otonkoski, R. Suuronen, O. Hovatta, and H. Skottman, "A defined and xeno-free culture method enabling the establishment of clinical-grade human embryonic, induced pluripotent and adipose stem cells", *PLOS ONE*, 2010. DOI: 10.1371/journal.pone.0010246.

[11] K. Takahashi, K. Tanabe, M. Ohnuki, M. Narita, T. Ichisaka, K. Tomoda, and S. Yamanaka, "Induction of Pluripotent Stem Cells from Adult Human Fibroblasts by Defined Factors", *Cell*, 2007. DOI: 10.1016/J.CELL.2007.11.019.

[12] J. Yu, M. A. Vodyanik, K. Smuga-Otto, J. Antosiewicz-Bourget, J. L. Frane, S. Tian, J. Nie, G. A. Jonsdottir, V. Ruotti, R. Stewart, I. I. Slukvin, and J. A. Thomson, "Induced pluripotent stem cell lines derived from human somatic cells", *Science*, 2007. DOI: 10.1126/science.1151526.

[13] G. Lemke, Ed., *Developmental Neurobiology 1st Edition*. Academic Press, 2009.

[14] P. A. Wilson and A. Hemmati-Brivanlou, "Induction of epidermis and inhibition of neural fate by Bmp-4", *Nature*, 1995. DOI: 10.1038/376331a0.

[15] I. Muñoz-Sanjuán and A. H. Brivanlou, "Neural induction, the default model and embryonic stem cells", *Nature Reviews Neuroscience*, 2002. DOI: 10.1038/nrn786.

[16] A. Zirra, S. Wiethoff, and R. Patani, "Neural Conversion and Patterning of Human Pluripotent Stem Cells: A Developmental Perspective", *Stem Cells International*, 2016. DOI: 10.1155/2016/8291260.

[17] L. M. Farkas and W. B. Huttner, "The cell biology of neural stem and progenitor cells and its significance for their proliferation versus differentiation during mammalian brain development", *Current Opinion in Cell Biology*, 2008. DOI: 10.1016/j.ceb.2008.09.008.

[18] R. S. Lappalainen, M. Salomäki, L. Ylä-Outinen, T. J. Heikkilä, J. A. Hyttinen, H. Pihlajamäki, R. Suuronen, H. Skottman, and S. Narkilahti, "Similarly derived and cultured hESC lines show variation in their developmental potential towards neuronal cells in long-term culture", *Regenerative Medicine*, 2010. DOI: 10.2217/rme.10.58.

[19] K. R. Koehler, P. Tropel, J. W. Theile, T. Kondo, T. R. Cummins, S. Viville, and E. Hashino, "Extended passaging increases the efficiency of neural differentiation from induced pluripotent stem cells", *BMC Neuroscience*, 2011. DOI: 10.1186/1471-2202-12-82.

[20] E. Abranches, M. Silva, L. Pradier, H. Schulz, O. Hummel, D. Henrique, and E. Bekman, "Neural differentiation of embryonic stem cells in vitro: A road map to neurogenesis in the embryo", *PLOS ONE*, 2009. DOI: 10.1371/journal.pone.0006286.

[21] K. Muguruma and Y. Sasai, "In vitro recapitulation of neural development using embryonic stem cells: From neurogenesis to histogenesis", *Development Growth and Differentiation*, 2012. DOI: 10.1111/j.1440-169X.2012.01329.x.

[22] T. F. Weiss, *Cellular Biophysics. Volume 2: Electrical Properties.* MIT Press, 1996.

[23] A. L. Hodgkin and A. F. Huxley, "A quantitative description of membrane current and its application to conduction and excitation in nerve", *The Journal of physiology*, 1952. DOI: 10.1113/jphysiol.1952.sp004764.

[24] M. E. J. Obien, K. Deligkaris, T. Bullmann, D. J. Bakkum, and U. Frey, "Revealing neuronal function through microelectrode array recordings", *Frontiers in Neuroscience*, 2015. DOI: 10.3389/fnins.2014.00423.

[25] A. Stett, U. Egert, E. Guenther, F. Hofmann, T. Meyer, W. Nisch, and H. Haemmerle, "Biological application of microelectrode arrays in drug discovery and basic research", *Analytical and Bioanalytical Chemistry*, 2003. DOI: 10.1007/s00216-003-2149-x.

[26] Multi Channel Systems MCS GmbH. (2019). MEA2100-System layout, [Online]. Available: https://www.multichannelsystems.com/products/mea2100-systems#description (visited on 05/28/2019).

[27] P. L. Nunez and R. Srinivasan, *Electric Fields of the Brain : The neurophysics of EEG 2nd Edition*. Oxford University Press, 2006. DOI: 10.1093/acprof:oso/9780195050387.001.0001.

[28] G. Buzsáki, C. A. Anastassiou, and C. Koch, "The origin of extracellular fields and currents-EEG, ECoG, LFP and spikes", *Nature Reviews Neuroscience*, 2012. DOI: 10.1038/nrn3241.

[29] D. A. Henze, Z. Borhegyi, J. Csicsvari, A. Mamiya, K. D. Harris, and G. Buzsáki, "Intracellular features predicted by extracellular recordings in the hippocampus in vivo.", *Journal of neurophysiology*, 2000. DOI: 10.1152/jn.2000.84.1.390.

[30] U. Egert, D. Heck, and A. Aertsen, "Two-dimensional monitoring of spiking networks in acute brain slices", *Experimental Brain Research*, 2002. DOI: 10.1007/s00221-001-0932-5.

[31] F. Lieb, H. G. Stark, and C. Thielemann, "A stationary wavelet transform and a time-frequency based spike detection algorithm for extracellular recorded data", *Journal of Neural Engineering*, 2017. DOI: 10.1088/1741-2552/aa654b.

[32] A. Belitski, A. Gretton, C. Magri, Y. Murayama, M. A. Montemurro, N. K. Logothetis, and S. Panzeri, "Low-Frequency Local Field Potentials and Spikes in Primary Visual Cortex Convey Independent Visual Information", *Journal of Neuroscience*, 2008. DOI: 10.1523/JNEUROSCI.0009-08.2008.

[33] R. Quian Quiroga, "What is the real shape of extracellular spikes?", *Journal of neuroscience methods*, 2009. DOI: 10.1016/j.jneumeth.2008.09.033.

[34] M. E. J. Obien, A. Hierlemann, and U. Frey, "Factors affecting blind localization of a glass micropipette using a high-density microelectrode array", in *Proceedings of IEEE Sensors*, 2013. DOI: 10.1109/ICSENS.2013.6688361.

[35] C. Gold, D. A. Henze, and C. Koch, "Using extracellular action potential recordings to constrain compartmental models", *Journal of Computational Neuroscience*, 2007. DOI: 10.1007/s10827-006-0018-2.

[36] M. Frega, M. Tedesco, P. Massobrio, M. Pesce, and S. Martinoia, "Network dynamics of 3D engineered neuronal cultures: A new experimental model for in-vitro electrophysiology", *Scientific Reports*, 2014. DOI: 10.1038/srep05489.

[37] I. Smith, V. Silveirinha, J. L. Stein, L. de la Torre-Ubieta, J. A. Farrimond, E. M. Williamson, and B. J. Whalley, "Human neural stem cell-derived cultures in three-dimensional substrates form spontaneously functional neuronal networks", *Journal of Tissue Engineering and Regenerative Medicine*, 2017. DOI: 10.1002/term.2001.

[38] N. Nabar and K. Rajgopal, "A wavelet based teager energy operator for spike detection in microelectrode array recordings", in *IEEE Region 10 Annual International Conference, Proceedings/TENCON*, 2009. DOI: 10.1109/TENCON.2009.5395915.

[39] J. H. Choi, H. K. Jung, and T. Kim, "A new action potential detector using the MTEO and its effects on spike sorting systems at low signal-to-noise ratios", *IEEE Transactions on Biomedical Engineering*, 2006. DOI: 10.1109/TBME.2006.870239.

[40] K. H. Kim and S. J. Kim, "Neural spike sorting under nearly 0-dB signal-to-noise ratio using nonlinear energy operator and artificial neural-network classifier", *IEEE Transactions on Biomedical Engineering*, 2000. DOI: 10.1109/10.871415.

[41] K. Mirfakhraei and K. Horch, "Classification of Action Potentials in MultiUnit Intrafascicular Recordings Using Neural Network Pattern-Recognition Techniques", *IEEE Transactions on Biomedical Engineering*, 1994. DOI: 10.1109/10.277276.

[42] I. L. Jones, P. Livi, M. K. Lewandowska, M. Fiscella, B. Roscic, and A. Hierlemann, "The potential of microelectrode arrays and microelectronics for biomedical research and diagnostics", *Analytical and Bioanalytical Chemistry*, 2011. DOI: 10.1007/s00216-010-3968-1.

[43] R. Quian Quiroga, Z. Nadasdy, and Y. Ben-Shaul, "Unsupervised spike detection and sorting with wavelets and superparamagnetic clustering", *Neural Computation*, 2004. DOI: 10.1162/089976604774201631.

[44] B. Lefebvre, P. Yger, and O. Marre, "Recent progress in multi-electrode spike sorting methods", *Journal of Physiology Paris*, 2016. DOI: 10.1016/j.jphysparis.2017.02.005.

[45] J. L. Semmlow and B. Griffel, *Biosignal and Biomedical Image Processing 3rd Edition*. CRC Press, 2014.

[46] J. R. Winkler, "Orthogonal Wavelets via Filter Banks: Theory and Applications", *The University of Sheffield, Department of Computer Science, Sheffield, United Kingdom*, 2000.

[47] Wikipedia contributors. (2019). Discrete wavelet transform – Wikipedia, The Free Encyclopedia, [Online]. Available: https://en.wikipedia.org/w/index.php?title=Discrete_wavelet_transform&oldid=891075598 (visited on 05/08/2019).

[48] J. E. Fowler, "The redundant discrete wavelet transform and additive noise", *IEEE Signal Processing Letters*, 2005. DOI: 10.1109/LSP.2005.853048.

[49] V. Shalchyan, W. Jensen, and D. Farina, "Spike detection and clustering with unsupervised wavelet optimization in extracellular neural recordings", *IEEE Transactions on Biomedical Engineering*, 2012. DOI: 10.1109/TBME.2012.2204991.

[50] Wikipedia contributors. (2019). Stationary wavelet transform – Wikipedia, The Free Encyclopedia, [Online]. Available: https://en.wikipedia.org/w/index.php?title=Stationary_wavelet_transform&oldid=887639490 (visited on 05/10/2019).

[51] P. Maragos, T. F. Quatieri, and J. F. Kaiser, "On Amplitude and Frequency Demodulation Using Energy Operators", *IEEE Transactions on Signal Processing*, 1993. DOI: 10.1109/78.212729.

[52] S. Mukhopadhyay and G. C. Ray, "A new interpretation of nonlinear energy operator and its efficacy in spike detection", *IEEE Transactions on Biomedical Engineering*, 1998. DOI: 10.1109/10.661266.

[53] J. Choi and T. Kim, "Neural action potential detector using multi-resolution TEO", *Electronics Letters*, 2002. DOI: 10.1049/el:20020386.

[54] A. Maccione, M. Gandolfo, P. Massobrio, A. Novellino, S. Martinoia, and M. Chiappalone, "A novel algorithm for precise identification of spikes in extracellularly recorded neuronal signals", *Journal of Neuroscience Methods*, 2009. DOI: 10.1016/j.jneumeth.2008.09.026.

[55] M. Natora, F. Franke, and K. Obermayer, "Spike detection in extracellular recordings by hybrid blind beamforming", in *2010 Annual International Conference of the IEEE Engineering in Medicine and Biology Society, EMBC'10*, 2010. DOI: 10.1109/IEMBS.2010.5626483.

[56] M. Mayer, O. Arrizabalaga, F. Lieb, M. Ciba, S. Ritter, and C. Thielemann, "Electrophysiological investigation of human embryonic stem cell derived neurospheres using a novel spike detection algorithm", *Biosensors and Bioelectronics*, 2018. DOI: 10.1016/j.bios.2017.09.034.

[57] H. Azami, J. Escudero, A. Darzi, and S. Sanei, "Extracellular spike detection from multiple electrode array using novel intelligent filter and ensemble fuzzy decision making", *Journal of Neuroscience Methods*, 2015. DOI: 10.1016/j.jneumeth.2014.10.006.

[58] K. H. Kim and S. J. Kim, "A wavelet-based method for action potential detection from extracellular neural signal recording with low signal-to-noise ratio", *IEEE Transactions on Biomedical Engineering*, 2003. DOI: 10.1109/TBME.2003.814523.

[59] J. Martinez, C. Pedreira, M. J. Ison, and R. Quian Quiroga, "Realistic simulation of extracellular recordings", *Journal of Neuroscience Methods*, 2009. DOI: https://doi.org/10.1016/j.jneumeth.2009.08.017.

[60] L. S. Smith and N. Mtetwa, "A tool for synthesizing spike trains with realistic interference", *Journal of Neuroscience Methods*, 2007. DOI: 10.1016/j.jneumeth.2006.06.019.

[61] R. Chandra and L. M. Optican, "Detection, classification, and superposition resolution of action potentials in multiunit single-channel recordings by an online real-time neural network", *IEEE Transactions on Biomedical Engineering*, 1997. DOI: 10.1109/10.568916.

[62] Axion BioSystems. (2019). Axion MEA, [Online]. Available: https://www.axionbiosystems.com/products (visited on 05/28/2019).

[63] H. Skottman, "Derivation and characterization of three new human embryonic stem cell lines in Finland", *In Vitro Cellular and Developmental Biology - Animal*, 2010. DOI: 10.1007/s11626-010-9286-2.

[64] K. Rajala, H. Hakala, S. Panula, S. Aivio, H. Pihlajamäki, R. Suuronen, O. Hovatta, and H. Skottman, "Testing of nine different xeno-free culture media for human embryonic stem cell cultures", *Human Reproduction*, 2007. DOI: 10.1093/humrep/del523.

[65] H. Hongisto, T. Ilmarinen, M. Vattulainen, A. Mikhailova, and H. Skottman, "Xeno- and feeder-free differentiation of human pluripotent stem cells to two distinct ocular epithelial cell types using simple modifications of one method", *Stem Cell Research and Therapy*, 2017. DOI: 10.1186/s13287-017-0738-4.

[66] Y. Shi, P. Kirwan, J. Smith, H. P. Robinson, and F. J. Livesey, "Human cerebral cortex development from pluripotent stem cells to functional excitatory synapses", *Nature Neuroscience*, 2012. DOI: 10.1038/nn.3041.

[67] S. Shahid and L. Smith, "Assessing new techniques for Spike Detection on MEA data", *6th International Meeting on Substrate-Integrated Micro Electrode Arrays*, 2008.

[68] Q. Wang, S. Yu, A. Simonyi, G. Y. Sun, and A. Y. Sun, "Kainic acid-mediated excitotoxicity as a model for neurodegeneration", *Molecular Neurobiology*, 2005. DOI: 10.1385/MN:31:1-3:003.

[69] D. Eytan and S. Marom, "Dynamics and effective topology underlying synchronization in networks of cortical neurons", *Journal of Neuroscience*, 2006. DOI: 10.1523/JNEUROSCI.1627-06.2006.